LLNL-JRNL-568497

LAWRENCE
LIVERMORE
NATIONAL
LABORATORY

Polymorphism and Melt in High-Pressure Tantalum

Justin B. Haskins, John A. Moriarty and Randolph Q. Hood

August 8, 2012

Submitted for publication in Physical Review B

Disclaimer

This document was prepared as an account of work sponsored by an agency of the United States government. Neither the United States government nor Lawrence Livermore National Security, LLC, nor any of their employees makes any warranty, expressed or implied, or assumes any legal liability or responsibility for the accuracy, completeness, or usefulness of any information, apparatus, product, or process disclosed, or represents that its use would not infringe privately owned rights. Reference herein to any specific commercial product, process, or service by trade name, trademark, manufacturer, or otherwise does not necessarily constitute or imply its endorsement, recommendation, or favoring by the United States government or Lawrence Livermore National Security, LLC. The views and opinions of authors expressed herein do not necessarily state or reflect those of the United States government or Lawrence Livermore National Security, LLC, and shall not be used for advertising or product endorsement purposes.

Polymorphism and Melt in High-Pressure Tantalum

Justin B. Haskins[1], John A. Moriarty[2] and Randolph Q. Hood[2]

[1]Artie McFerrin Department of Chemical Engineering, Texas A&M University, College Station, Texas 77843-1372 USA

[2]Condensed Matter and Materials Division, Lawrence Livermore National Laboratory, Livermore, California 94551-0808 USA

Abstract

Recent small-cell (< 150-atom) quantum molecular dynamics (QMD) simulations for Ta based on density functional theory (DFT) have predicted a hexagonal omega (hex-ω) phase more stable than the normal bcc phase at high temperature (T) and pressure (P) above 70 GPa [Burakovsky *et al*., Phys. Rev. Lett. **104**, 255702 (2010)]. Here we examine possible high-T,P polymorphism in Ta with complementary DFT-based model generalized pseudopotential theory (MGPT) multi-ion interatomic potentials, which allow accurate treatment of much larger system sizes (up to ~ 80000 atoms). We focus on candidate bcc, A15, fcc, hcp, and hex-ω phases for the high-T,P phase diagram to 420 GPa, studying the mechanical and relative thermodynamic stability of these phases for both small and large computational cells. Our MGPT potentials fully capture the $T=0$ DFT energetics of these phases, while MGPT-MD simulations demonstrate that the higher-energy fcc, hcp and hex-ω structures are only mechanically stabilized at high temperature by large, size-dependent, anharmonic vibrational effects, with the stability of the hex-ω phase also being found to be a sensitive function of its c/a ratio. Both two-phase and Z-method melting techniques have been used in MGPT-MD simulations to determine relative phase stability and its size dependence. In the large-cell limit, the two-phase method yields accurate equilibrium melt curves for all five phases, with bcc producing the highest melt temperatures at all pressures and hence being the most stable phase of those considered. The two-phase bcc melt curve is also in good agreement with dynamic experimental data as well as with the MGPT melt curve calculated from bcc and

liquid free energies. In contrast, we find that the Z method produces only an upper bound to the equilibrium melt curve in the large-cell limit. For the bcc and hex-ω structures, however, this is a close upper bound within 5% of the two-phase results, although for the A15, fcc, and hcp structures, the Z-melt curves are 25-35% higher in temperature than the two-phase results. Nonetheless, the Z method has allowed us to study melt size effects in detail. We find these effects to be either small or modest for the cubic bcc, A15, and fcc structures, but to have a large impact on the hexagonal hcp and hex-ω melt curves, which are dramatically pushed above that of bcc for simulation cells less than a 150 atoms. The melt size effects are driven by and closely correlated with similar size effects on the mechanical stability and the vibrational anharmonicity. We further show that for the same simulation cell sizes and choice of c/a ratio, the MGPT-MD bcc and hex-ω melt curves are in good agreement with the QMD results, so the QMD prediction is confirmed in the small-cell limit. But in the large-cell limit, the MGPT-MD hex-ω melt curve is always lowered below that of bcc for any choice of c/a, so bcc is the most stable phase. We conclude that for the non-bcc Ta phases studied, one requires simulation cells of at least 250-500 atoms to be free of size effects impacting mechanical and thermodynamic phase stability.

PACS: 81.30.Bx, 64.70.D-, 64.60.My, 71.15.Pd

I. INTRODUCTION

At ambient pressure, high-temperature polymorphism in the 5*d* bcc metals tantalum (Ta) and tungsten (W) has been of long-standing historical interest because of the presence of a mechanically stable and energetically competitive A15 structure [1,2], which is well known to occur in the phase diagrams of respective group-VB and -VIB binary compounds and alloys. In elemental W, the A15 structure can be realized by the hydrogen reduction of WO_3 and is alternatively known as the β-W structure [3]. In elemental Ta, experimental evidence indicates that an A15 phase can be solidified from the supercooled liquid [1], and quantum-based atomistic simulations [2,4], using molecular dynamics (MD) with model generalized pseudopotential theory (MGPT) interatomic potentials [2,5,6], have confirmed the intense competition between the bcc and A15 structures during rapid solidification.

More recently, research interest in high-temperature polymorphism in the bcc transition metals has re-emerged in connection with unexpected results from static high-pressure melting experiments, where laser-heated diamond-anvil-cell (DAC) measurements on V [7], Ta [7,8], Mo [7,9] and W [7] have indicated only small increases in the melting temperature T_{m} with increasing melting pressure P_{m} up to 100 GPa. These flat $T_{\mathrm{m}}(P_{\mathrm{m}})$ melt curves strongly conflict with the steep melt curves indicated by dynamic experimental data, namely, the large melting slopes $dT_{\mathrm{m}}/dP_{\mathrm{m}}$ obtained for Nb [10], Ta [11,12], Mo [11] and W [12,13] at low pressure from isobaric expansion measurements and the high shock melt temperatures at high pressure obtained for V at 225 GPa [14], Ta at 295 GPa [15,16] and Mo at 390 GPa [17] from sound velocity measurements and either calculated equations of state [14,15,17] or a measured shock temperature via pyrometry [16]. In each case, at the observed shock melt pressure, the estimated shock melt temperature is at least a factor of two greater than the melt temperature extrapolated from the DAC data. Moreover, recent theoretical melting results for Ta [2,18-22] and Mo [23-25], based on either first-principles density-functional-theory (DFT) [26] data input into various melt methodologies or direct DFT calculation, have all produced steep melt curves in qualitative agreement with the dynamic data.

The conflict between flat and steep melt curves in bcc transition metals has led to a decade of controversy concerning the correct interpretation of the DAC measurements, with considerable follow-up research on the high-T,P phase diagram in these materials, including theoretical evidence for possible undiscovered phases and solid-solid phase transitions prior to melt [22,24,25,27] and an alternative DAC measurement that yields a much steeper $T_{\mathrm{m}}(P_{\mathrm{m}})$ melt curve in Ta [28]. Recent DFT-based quantum molecular dynamics (QMD) simulations in Ta [22] and Mo [24] have predicted that there is at least one additional solid phase more stable than bcc in each material under high-T,P conditions. In the case of Mo, a stable high-temperature fcc phase above 150 GPa has been found to be possible [24], and this might explain an observed break in the measured sound velocity near 210 GPa [17] prior to shock melt at 390 GPa. In the case of Ta, a stable high-temperature hexagonal omega (hex-ω) phase above 70 GPa has been found possible that is consistent with a bcc → hex-ω transition on the shock Hugoniot near 100 GPa [22], where a similar break in the measured sound velocity is indicated [15,22] prior to shock melt at 295 GPa. The presence of a hex-ω phase has also been reported in a shock-recovered Ta sample [29], although the material was shocked to only 45 GPa and ~ 550 K. In addition, MGPT-MD simulations on Ta under an applied shear stress [27] have revealed that the bcc structure undergoes an order to partial disorder transition at the temperature and pressure conditions of the original DAC melt measurements [7,8]. This behavior was interpreted as a Bingham-like plastic flow and is consistent with both the elastic softening of the bcc structure found in an earlier MGPT study of high-T,P elasticity in Ta [30] and the general conditions needed for the appearance of other mechanically stable and energetically competitive structures.

Perhaps the most interesting and challenging aspect of high-T,P polymorphism in the bcc transition metals is that the structural-energy landscape in these materials at high temperature is completely different than at low temperature. At zero temperature, the bcc structure is very stable both mechanically and thermodynamically, and with the exception of the A15 structure in Ta and W near ambient pressure, all other structures are much higher in energy and unstable mechanically. In the case of Ta, this has been quite clearly demonstrated with first-principles DFT calculations, where the bcc structure is predicted

to be the stable phase to at least 1000 GPa [22,31], while alternate A15, hex-ω, fcc, hcp and dhcp structures all have calculated imaginary quasi-harmonic phonon frequencies over this pressure range [22]. The latter elastically soft structures are only mechanically stabilized at high temperature by large anharmonic vibrational effects (phonon-phonon interactions), and become competitive with bcc via the equally large effect of temperature on the underlying electronic structure, which strongly impacts the free-energy differences between phases. Accurate modeling of high-T,P phase stability and polymorphism in bcc transition metals thus requires not only robust quantum mechanics, but robust statistical mechanics and free-energy determination as well. In this regard, QMD and MGPT-MD simulations are largely complementary. In principle, DFT-based QMD simulations provide robust quantum mechanics, but these simulations are rather severely limited by computational cell size and time scale. In the Ta and Mo QMD polymorphism studies [22,24], for example, the simulation cell sizes considered were only between 32 and 144 atoms. In the MGPT approach [2,5,6], on the other hand, the DFT quantum-mechanical framework is retained, but the electronic structure is effectively course-grained by a multi-ion expansion of the total-energy functional, which is truncated beyond four-ion interactions. In MGPT-MD simulations, this allows one to capture the crucial DFT quantum mechanics, while providing up to six orders of magnitude increase in computational speed over QMD and hence the possibility of much more robust statistical mechanics in polymorphism studies, with no important limitations on either cell size or simulation duration.

Deriving free energies directly from QMD simulations is also extremely difficult and such energies are not available for Ta or Mo phases. On the other hand, an efficient MGPT-MD free-energy scheme has been developed and applied to the stable bcc and liquid phases of Ta [32]. This scheme is currently being extended to metastable solid phases as well, but free-energy data does not yet exist for any of the possible polymorphic structures. In lieu of free-energy data, dynamic melting methods can be used in either the QMD or MGPT-MD approaches as a means of determining the relative stability of different solid phases. Specifically, for any high-temperature mechanically stable phase the temperature can be raised and a melt point determined. At a given

pressure, the solid phase with the highest melt temperature is judged to be the most thermodynamically stable phase. Two dynamic melt methods that can be so applied to polymorphism studies are the well-known two-phase coexistence method due originally to Morris *et al*. [33] and the more recent so-called Z method of Belonoshko *et al.* [34]. The latter purports to offer a shortcut useful for QMD simulations and was the principal melt method used in the Ta and Mo polymorphism studies [22,24].

The primary purpose of the present paper is to report a comprehensive study of polymorphism and high-pressure melt in Ta using the MGPT-MD approach. To compare and contrast our results with the recent QMD study in Ta [22], we consider melt out of the bcc, A15, fcc, hcp and hex-ω solid phases with both small and large computational cells and with both the two-phase and Z melt methods. A few Z-method MGPT-MD melt results were previously reported in Ref. 22 based on version-4 MGPT potentials (denoted here as Ta4), which have also been used in other recent Ta applications [4,6,21,25,27,30]. In Sec. II we briefly review the MGPT method and discuss the latest version-6.8*x* Ta MGPT potentials [32] used in the present study. These potentials, denoted here as Ta6.8*x*, represent a useful systematic numerical improvement over the Ta4 potentials. We also discuss in Sec. II our specific implementations of the two-phase and Z melt methods, and benchmark bcc melt curves obtained from those methods against one obtained directly from free energies. Then in Sec. III we consider the low- and high-temperature mechanical stability of the five solid phases treated in this paper. We quantify the quality of the mechanical stability achieved in our simulations of these phases at high temperature via accurate calculation of the stress tensor. We also quantify the degree of anharmonic vibrational behavior exhibited in each phase at high temperature. Next in Sec. IV we assess the importance of size effects and melt method for each of the five candidate phases. We obtain large-cell MGPT-MD predictions of relative phase stability with both the two-phase and Z methods, while reconciling small-cell QMD and MGPT-MD results. Finally, we conclude in Sec. V and discuss the implications of our results for the Ta high-pressure phase diagram.

II. THEORETICAL and COMPUTATIONAL METHODS

In this section we first briefly review the origin and framework of the MGPT method, and discuss the specific Ta6.8*x* potentials used in the present work. We then discuss the methods of melt calculation to be used in determining relative phase stability for the different possible polymorphs. We include in the latter discussion determination of the bcc melt curve from bcc and liquid free energies as a benchmark for the dynamic two-phase and Z methods.

A. MGPT interatomic potentials

Within DFT quantum mechanics, generalized pseudopotential theory (GPT) provides a fundamental approach to first-principles interatomic potentials in transition metals [35]. In the GPT, a mixed wave-function basis of plane waves and localized, atomic-like *d* states is used to expand the electron density and total energy of the system in terms of weak *sp* pseudopotential, *d-d* tight-binding, and *sp-d* hybridization matrix elements, which effectively couple different ion sites. For a bulk metal at atomic volume Ω, one derives a real-space total-energy functional of the *N* ion positions $\mathbf{R} \equiv \{\mathbf{R}_i\}$ in the form

$$E_{\text{tot}}(\mathbf{R};\Omega) = NE_{\text{vol}}(\Omega) + \frac{1}{2}\sum_{i,j}{}' v_2(ij;\Omega) + \frac{1}{6}\sum_{i,j,k}{}' v_3(ijk;\Omega) + \frac{1}{24}\sum_{i,j,k,l}{}' v_4(ijkl;\Omega) \ , \qquad (1)$$

where the prime on each summation sign denotes the exclusion of all self-interaction terms from the summation. The leading volume term in this expansion E_{vol} as well as the two-, three-, and four-ion interatomic potentials, v_2, v_3, and v_4, depend explicitly on atomic volume but are structure independent and transferable to all bulk ion configurations, either ordered or disordered. This includes all possible structural phases as well as the imperfect solid with point and extended defects present. The angular-force multi-ion potentials v_3 and v_4 in Eq. (1) reflect directional bonding contributions from partially filled *d* bands and are important for the mid-period transition metals. In the full first-principles GPT, however, v_3 and v_4 are generally long-ranged, multidimensional functions that cannot be tabulated for application purposes, and need to be recalculated at

each usage. To overcome this limitation, the simplified *model* GPT or MGPT has been developed for bcc transition metals [5] in which shorter-ranged, analytic potential forms are achieved for v_3 and v_4 that can be readily applied to large-scale atomistic simulations [2,5,6].

The MGPT is derived from the GPT through a series of systematic approximations applicable to mid-period transition metals with nearly half-filled *d* bands. Equation (1) for the total-energy functional is maintained in the MGPT but the multi-ion potentials v_2, v_3, and v_4 are simplified in three main steps. First, it is noted that the *sp*-*d* hybridization contributions to the potentials destructively interfere for half-filled *d* bands, so these contributions are neglected. Second, highly symmetrical canonical *d* bands [5] are introduced to allow the remaining *d*-state band-structure contributions to the potentials to be evaluated analytically in terms of a single radial function $f(r)$ and three universal angular functions *L*, *P* and *M*, which depend only on *d* symmetry [5]. Finally, additional multi-ion *d*-state non-orthogonality contributions are folded back into v_2 as part of a short-ranged repulsive "hard-core" potential v_2^{hc}. The two-ion pair potential in the MGPT then has the form

$$v_2(r,\Omega) = v_2^{sp}(r,\Omega) + v_2^{\mathrm{hc}}(r,\Omega) + v_a(\Omega)[f(r)]^4 - v_b(\Omega)[f(r)]^2 \ , \tag{2}$$

where v_2^{sp} is an *sp* pseudopotential contribution, and v_a and v_b are volume-dependent *d*-band coefficients. Here $f(r) = (1.8R_{WS}/r)^p$, where R_{WS} is the Wigner-Seitz radius and *p* is a weakly volume-dependent parameter optimized in the range 4-6, with a Gaussian cutoff introduced beyond the bcc second-neighbor distance. For pure canonical *d* bands, $p = 2\ell + 1 = 5$ with $\ell = 2$, but in Ta applications we have taken $p = 4$ at the observed equilibrium volume $\Omega_0 = 121.6$ a.u., with *p* increasing monotonically for decreasing Ω.

The three- and four-ion potentials in the MGPT contain correspondingly simplified multi-ion *d*-band contributions and can be written in terms of three and six radial distances, r_n, respectively, and dependent angles, θ_n:

$$v_3(r_1,r_2,r_3;\Omega) = v_c(\Omega) f(r_1) f(r_2) f(r_3) L(\theta_1,\theta_2,\theta_3) + v_d(\Omega)\{[f(r_1)f(r_2)]^2 P(\theta_3) + [f(r_2)f(r_3)]^2 P(\theta_1) + [f(r_3)f(r_1)]^2 P(\theta_2)\} \quad (3)$$

and

$$v_4(r_1,r_2,r_3,r_4,r_5,r_6;\Omega) = v_e(\Omega)[f(r_1)f(r_2)f(r_3)f(r_4)M(\theta_1,\theta_2,\theta_3,\theta_4,\theta_5,\theta_6) + f(r_3)f(r_2)f(r_6)f(r_5)M(\theta_7,\theta_8,\theta_9,\theta_{10},\theta_5,\theta_{12}) + f(r_1)f(r_6)f(r_4)f(r_3)M(\theta_{11},\theta_{12},\theta_5,\theta_6,\theta_3,\theta_4)] \quad , \quad (4)$$

where v_c, v_d, and v_e are additional volume-dependent *d*-band coefficients. The specific three- and four-ion geometries assumed in Eqs. (3) and (4) are defined in Figs. 4a and 6, respectively, of the first paper in Ref. [5].

In the MGPT, the two-ion potential contributions v_2^{sp} and v_2^{hc} in Eq. (2) are determined from first-principles, as in the full GPT. The remaining five *d*-band coefficients v_a, v_b, v_c, v_d, and v_e in Eqs. (2)-(4) are also well-defined material parameters that depend on *d*-band filling and width. However, to compensate for the approximations introduced into the MGPT, these latter quantities, together with the volume term E_{vol} in Eq. (1), are fit to a combination of experimental and first-principles DFT data on basic material properties, subject to the theoretical constraints $v_b \gg v_a > 0$ and $v_e > v_d > v_a > 0$. Specifically for the group-VB and -VIB metals, we fit, as a function of volume in the bcc phase, a blend of experimental data at ambient pressure and DFT data at high pressure on the cold equation of state, shear elastic moduli, *unrelaxed* vacancy formation energy, and the Debye temperature, subject to the additional constraint of the compressibility sum rule, which reduces the number of independent parameters from six to five. In the case of Ta, we have refined this basic scheme over a number of generations of MGPT potentials, with the closely related Ta3 [2] and Ta4 [2,36] potentials being the first published versions. These latter two versions were developed over a wide pressure range extending to 1000 GPa and differ only in the treatment of input unrelaxed vacancy formation energies, which in Ta4 were uniformly shifted upward by 0.15 eV at all volumes from the values used in Ta3. With the Ta4 potentials, the calculated *relaxed* vacancy formation energy at ambient pressure is then in better agreement with both experiment and DFT calculations

[36], and the calculated melt curve [21,37] is significantly lowered, as discussed below in Sec. IIB1. In the present Ta6.8*x* potentials [32], three additional numerical refinements have been added to the Ta4 scheme. First, a smoother blend of the input experimental and DFT data has been used through explicit analytic representations of that data, although this restricts the effective high-pressure limit to about 420 GPa in Ta6.8*x*. Second, an improved analytic fit to the hard-core potential v_2^{hc} in Eq. (2) has been introduced. Finally, these latter two improvements have allowed the MGPT potentials to be defined on a finer volume mesh, producing more accurate calculated thermodynamics from quasi-harmonic lattice dynamics (QHLD) at low temperature and MGPT-MD simulations at high temperature.

B. Methods of melt calculation

As in other recent Ta4 MGPT applications [4,6,21,25,27,32], all of the melt methods discussed below apply the Ta6.8*x* potentials using the advanced matrix representation of MGPT [6], as implemented in the parallel molecular dynamics code *ddcMD* [38]. In *ddcMD*, the angular functions *L*, *P*, and *M* in Eqs. (3) and (4) are evaluated on the fly during an MGPT-MD simulation through *d*-state matrix multiplication, while the multi-ion forces that move the ions are determined analytically. This provides maximum computational efficiency and accuracy. The additional advanced MGPT features of non-canonical *d* bands and electron-temperature dependent potentials, recently developed and applied to the narrow *d*-band metal Mo [25], are much less important in wider-band 5*d* metals like Ta and are not included in Ta6.8*x*.

In addition, and as was the case in the recent Ta QMD simulations [22], all of the present MGPT-MD simulations have been performed in standard fixed-shape computational cells at constant volume. Cubic unit cells of 2, 4, and 8 atoms have been used for the bcc, fcc and A15 structures, respectively, while hexagonal unit cells of 2 and 3 atoms have been used for the hcp and hex-ω structures, respectively. Thus, for example, a 250-atom MGPT-MD simulation in the bcc phase corresponds to a cubic $5\times5\times5$ simulation cell. For the hcp and hex-ω structures, the internal c/a ratio has been treated as a fixed input structural parameter and has not been relaxed during the simulation.

1. Free energies

For Ta the thermodynamics of the system is well described by the conventional weak-coupling model, in which the Helmholtz free energy A_{tot} at volume Ω and temperature T is obtained as a sum of cold, ion-thermal, and electron-thermal contributions:

$$A_{\mathrm{tot}}(\Omega,T) = E_0(\Omega) + A_{\mathrm{ion}}(\Omega,T) + A_{\mathrm{el}}(\Omega,T) \ . \tag{5}$$

By the method of construction of the MGPT potentials, the cold energy E_0 is accurately described via Eq. (1) evaluated in the bcc structure at $T = 0$. The ion-thermal free-energy component A_{ion} in Eq. (5) can also be evaluated for the bcc and liquid phases of Ta from the MGPT potentials, as first described for Ta3 in Ref. [2]. For the Ta4 and Ta6.8*x* potentials, A_{ion} has been obtained using the new and more efficient free-energy scheme developed in Ref. [32]. This latter scheme, which utilizes the statistical mechanics principles of thermodynamic integration and reversible-scaling MD (RSMD) simulation [39], involves a combination of standard QHLD and MGPT-RSMD calculation of anharmonic contributions in the bcc solid, together with MGPT-RSMD calculation of corresponding ion-thermal contributions in the liquid. The final electron-thermal free-energy component A_{el} in Eq. (5) embodies the remaining effects of temperature on the structure and occupation of the electronic states of the system. While this contribution can and has been treated at different levels of approximation, an accurate treatment was developed in Ref. [2] in terms of configuration-averaged, finite-temperature DFT calculations in the bcc and liquid phases, using atomic configurations obtained from MGPT-MD simulations. The resulting electron-thermal contribution has been found to lower the calculated melt curve by only a small amount ($\leq 5\%$), however. This contribution has been retained nonetheless and used in reported MGPT free-energy melt-curve calculations, both in the previously published Ta3 [2] and Ta4 [21,37] results and with the present Ta6.8*x* result displayed in Figs. 1 and 2 below. In all subsequent results presented in this paper beyond Fig. 2, however, electron-thermal corrections are not included in the melt results.

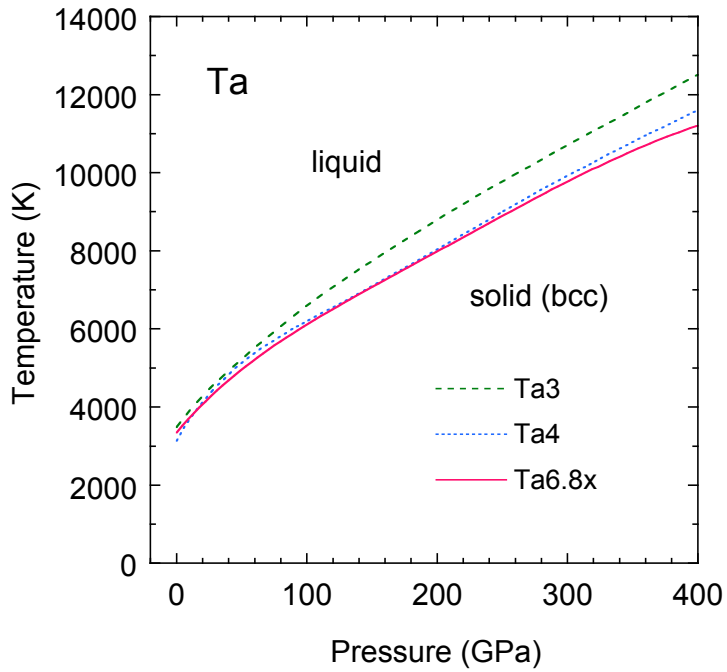

Fig. 1 High-pressure melt curve of Ta out of the bcc phase, as calculated from bcc and liquid free energies via Eq. (5), using Ta3, Ta4, and the present Ta6.8*x* MGPT multi-ion interatomic potentials.

Figure 1 compares the free-energy-calculated, high-pressure melt curves out of the bcc phase of Ta up to 400 GPa, as obtained with the Ta3, Ta4, and Ta6.8*x* MGPT potentials. In all three cases, the MGPT-MD simulations used to determine A_{ion} for the bcc and liquid phases were performed with 250-atom, constant-volume ensembles with periodic boundary conditions. The Ta4 melt curve is lowered significantly below the Ta3 result above 100 GPa, with the melt temperature at 400 GPa lower by about 1000 K. On the other hand, and as expected, the Ta4 and Ta6.8*x* melt results are quite close to one another, with the Ta6.8*x* melt curve calculated slightly lower, except near ambient pressure.

In Fig. 2 we compare our calculated Ta6.8*x* free-energy-based melt curve out of the bcc phase against the corresponding fitted QMD result of Burakovsky *et al.* [22], as well as against static [7,8,28] and dynamic [11,15,16] experimental data. The MGPT and QMD melt results are in good accord with each other and with the measured isobaric melt slope

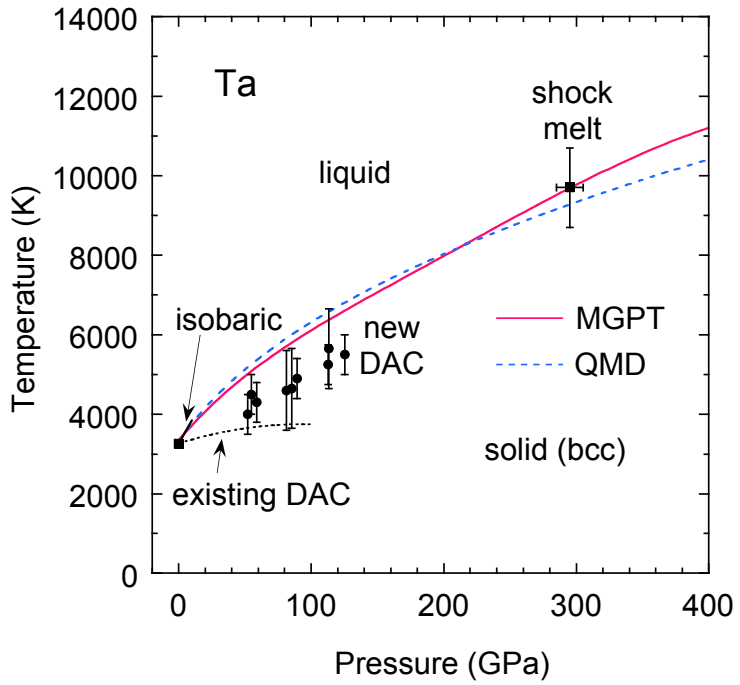

Fig. 2 High-pressure melting curve in Ta, as obtained from MGPT Ta6.8*x* free energies and QMD simulations [22] and compared with experimental data from both existing [7,8] and new [28] DAC measurements, and with data from isobaric [11] and shock [15,16] measurements.

at low pressure [11] and with the measured shock melt point at 295 GPa [15,16]. The flat melt curve obtained from existing DAC data [7,8], on the other hand, clearly diverges from the theoretical results with increasing pressure. The new DAC data of Dewaele *et al*. [28] is in much better agreement with theory, but still indicates significantly lower melt temperatures than the calculated values in the experimental 50-125 GPa pressure range. In the dynamic data, the structure of the melting solid phase is not determined, while in all of the DAC experiments the reported melting solid phase is bcc, with no solid-solid phase transition detected prior to melting.

2. Two-phase simulation

In the dynamic two-phase and Z melt methods as applied here, melting is determined entirely from the MGPT potentials via MD simulation without any correction for the small electron-thermal free energy included above in Eq. (5). The melt curves so

obtained thus correspond to solid and liquid free energies in the $A_{\mathrm{el}} = 0$ limit. Our two-phase melt method [25,37] is a robust version of the standard two-phase method of Morris *et al*. [33]. In this approach, equilibrated solid and liquid subcells of equal size and shape are placed in contact and the movement of the solid-liquid interface is monitored as a function of pressure for a trial melt temperature T_{m}. Periodic boundary conditions are applied to all remaining faces of the subcells. The equilibrium melting pressure $P_{\mathrm{m}}(T_{\mathrm{m}})$ is achieved when the solid-liquid interface remains stationary and neither the solid nor the liquid phase is growing at the expense of the other.

Our MGPT-MD two-phase simulation method is implemented with *ddcMD* in a series of three main steps for each melt temperature T_{m} considered. The first step is to run MGPT-MD subcell simulations to determine accurate solid and liquid pressure-volume relations at temperature T_{m} that are needed to equalize solid and liquid pressures in the full simulation cell. Constant temperature is maintained in *ddcMD* simulations with a special Langevin thermostat [4,38]. The next step is to initialize and run the full-cell two-phase simulations for a range of atomic volumes, each corresponding to a solid trial pressure $P_{\mathrm{tr}}(\Omega, T_{\mathrm{m}})$. For each volume Ω, we start with a bcc atomic arrangement of Ta atoms in the full cell and randomly remove the appropriate number of atoms from the liquid sub-cell such that the pressures of the solid and liquid phases will be equal to P_{tr} at temperature T_{m}. With the atoms in the solid subcell frozen, the liquid subcell is first briefly equilibrated at T_{m}, then melted at a high temperature (20000 K in the present Ta simulations), and finally cooled back to T_{m} as a liquid. We then allow all of the atoms in the full cell to move in an extended MGPT-MD simulation at pressure P_{tr} and accumulate statistics needed to indicate any movement of the solid-liquid interface.

The final step is to use the accumulated statistics to trace the movement of the solid-liquid interface as a function of $P_{\mathrm{tr}}(\Omega, T_{\mathrm{m}})$, or more precisely to determine the growth of the solid phase into the liquid if $P_{\mathrm{tr}} > P_{\mathrm{m}}$ or the growth of the liquid phase into the solid if $P_{\mathrm{tr}} < P_{\mathrm{m}}$. To do this, we employ a time-dependent short-range order parameter, $\mathrm{O}_{\ell}(t)$, defined for angular momentum ℓ as [40]

$$\mathrm{O}_\ell(t) = 4\pi \sum_m \left| \langle Y_{\ell m} \rangle \right|^2 / (2\ell+1) \ , \tag{6}$$

where

$$\langle Y_{\ell m} \rangle = \sum_{i,j} \Theta(r_{cut} - R_{ij}) Y_{\ell m}(\mathbf{R}_i - \mathbf{R}_j) \ , \tag{7}$$

with Θ a step function and r_{cut} a chosen cutoff radius. Specifically, we accumulate statistics for the $\ell = 6$ order parameter $\mathrm{O}_6(t)$ as a function of simulation time t. The parameter $\mathrm{O}_6(t)$ is near zero for the liquid phase and is a non-zero constant for the solid phase, so it will tend to one or the other as a given two-phase simulation proceeds. We obtain nearly linear plots of $\mathrm{O}_6(t)$ versus t until the two-phase system either completely melts or is completely solidified. For the atomic volumes Ω considered, the slopes of the $\mathrm{O}_6(t)$ curves are plotted versus Ω and fit to a quadratic equation. The atomic volume that produces a zero slope is taken as the solid melting atomic volume Ω_{m} at temperature T_{m}, such that $P_{\mathrm{m}} = P_{\mathrm{tr}}(\Omega_{\mathrm{m}}, T_{\mathrm{m}})$. This whole three-step process is repeated for as many melt temperatures as desired to obtain the two-phase $T_{\mathrm{m}}(P_{\mathrm{m}})$ melt curve.

The MGPT two-phase melt curve so obtained for Ta melting out of the bcc phase is displayed in Fig. 3 and compared with the corresponding free-energy result in the $A_{\mathrm{el}} = 0$ limit. These results and all remaining MGPT results reported below in this paper were obtained with the Ta6.8*x* potentials. The two-phase and free-energy melt curves in Fig. 3 are essentially identical below 100 GPa and differ only slightly by 1-2% above 100 GPa. We believe the latter difference is within the numerical error of either calculation. In this regard, the two-phase result shown was based on nine calculated melt pressures with an initial total of 78,732 atoms used in each simulation, corresponding to a $54 \times 27 \times 27$ full cell. While for two-phase melting out of the bcc structure, net size effects beyond 256 atoms ($8 \times 4 \times 4$ full cell) are negligible, the use of a large number of atoms greatly reduces the statistical error bars on each individual melt point, so that a smooth melt curve is obtained directly from the calculated points. The free-energy result, on the other hand, was obtained from 250-atom MGPT-RSMD simulations, as discussed above.

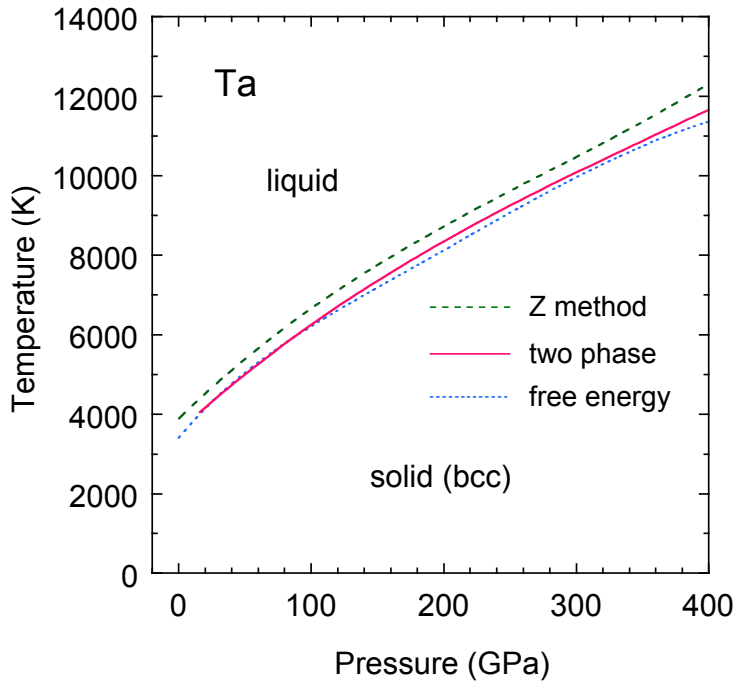

Fig. 3 High-pressure melt curve of Ta out of the bcc phase, as calculated with the present Z, two-phase, and free-energy methods using Ta6.8*x* MGPT potentials, but without correction for electron-thermal contributions, i.e., with $A_{\mathrm{el}} = 0$ in Eq. (5).

3. Z method

The Z method of Belonoshko *et al.* [34] attempts to connect the homogeneous melting of a solid at a critical temperature T_c, as obtained from superheating the material in an MD simulation at constant volume with periodic boundary conditions, to the true equilibrium melt temperature T_{m}. The underlying hypothesis of the method is that for such conditions the total energy of the solid $E_{\mathrm{tot}}^{\mathrm{sol}}$ at $T = T_c$ is equal to the total energy of the liquid $E_{\mathrm{tot}}^{\mathrm{liq}}$ at $T = T_{\mathrm{m}}$:

$$E_{\mathrm{tot}}^{\mathrm{sol}}(\Omega, T_c) = E_{\mathrm{tot}}^{\mathrm{liq}}(\Omega, T_{\mathrm{m}}) \ . \tag{8}$$

Belonoshko *et al.* [34] proposed a simple dynamic approach to implement the content of Eq. (8): perform a small sequence of MD simulations in a micro-canonical ensemble at constant energy and constant volume, adding kinetic energy to increase the temperature

in the solid phase until T_c is reached, and then watch the system spontaneously drop in temperature during melt to T_{m} in the liquid. Adding additional kinetic energy increases the temperature of the system in the liquid, so that on a temperature-pressure diagram the whole path followed resembles the letter Z. They successfully tested their method on a simple Lennard-Jones model of argon and an embedded-atom method (EAM) [41] model of copper. Additional shortcuts to implement the Z method have also been proposed and applied to QMD melt simulations [24]. Recently, Alfè *et al*. [42] did an extended analysis of the Z method in the context of EAM-MD and QMD melt simulations on iron. They found that there is a size-dependent waiting time for melt to occur after the critical point in the solid is reached, resulting in a strong tendency to overestimate T_c and T_{m} when the method is implemented with just a few simulations.

In our present use of the Z method, we are not directly concerned with either the efficiency or the specific methodology of the various constant-energy implementations of Eq. (8), but rather with the physical accuracy of this equation in determining the equilibrium melt temperature. As a result, we have implemented the Z method in an alternate way through a series of incremented solid and liquid MGPT-MD simulations using *ddcMD*, with each simulation performed in a canonical ensemble at constant temperature and constant volume to determine as accurately as possible the functions $E_{\mathrm{tot}}^{\mathrm{sol}}(\Omega,T)$ and $E_{\mathrm{tot}}^{\mathrm{liq}}(\Omega,T)$ together with the critical temperature T_c. We then solve Eq. (8) for T_{m}. An example of this approach is illustrated in Fig. 4 for melting out of the bcc phase of Ta at a single representative volume ($\Omega_0 = 121.6$ a.u.), with 250 atoms used in a periodic simulation cell. In this example, we ascended the solid portion of the Z curve with ~ 30 ps MGPT-MD simulations in increments of 500 K to 5000 K, at which point we increased the simulation duration to ~ 70 ps and reduced the temperature increment to 100 K until critical melting was encountered at 5100 K. To determine $E_{\mathrm{tot}}^{\mathrm{liq}}(\Omega,T)$, we first melted the bcc solid at high temperature and established a good equilibrium liquid state, and then similarly descended the liquid portion of the Z curve in increments of 500 K. We estimate that we thereby determine both T_c and T_{m} in Eq. (8) to an accuracy of about ± 100 K for a given MGPT potential. As can be seen in Fig. 4, our Z-calculated

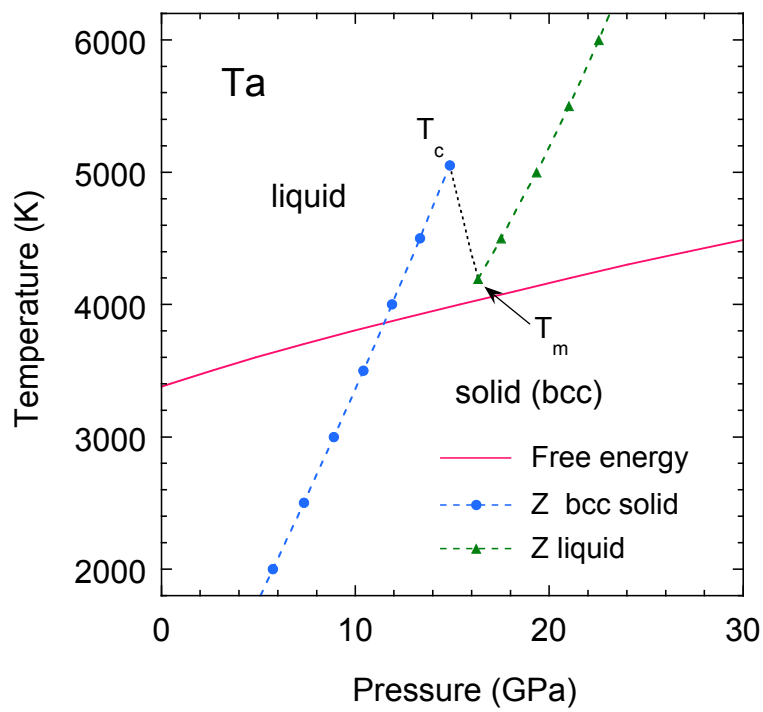

Fig. 4 Melt temperature T_m in bcc Ta at an atomic volume of 121.6 a.u., as determined from the present MGPT implementation of the Z method and as compared with the corresponding free-energy melt curve.

T_m still lies about 200 K or 5% above the corresponding free-energy calculated melt curve. A similar overestimate of T_m is found all along the bcc melt curve, as shown in Fig. 3, where the Z-method results were obtained with 2000-atom simulations (a $10\times10\times10$ computational cell). We thus conclude that the Z method as applied here to bcc Ta with MGPT potentials provides only a close upper bound to the equilibrium melt curve. We will further demonstrate in Sec. IV that the quantitative degree of the upper bound is dependent on the detailed nature of the solid melting phase. At the same time, the Z method is readily applicable to both small and large computational cells, so that it is a convenient approach to study size effects on the melt curve for the remaining candidate polymorphic phases.

III. HIGH-TEMPERATURE MECHANICAL STABILITY of SOLID PHASES

In this section we discuss the mechanical stability of our five identified candidate high-T,P solid phases of Ta: bcc, A15, fcc, hcp, and hex-ω. In this regard, the hcp and hex-ω structures also have an internal c/a parameter to consider. For the hcp structure, we fix this parameter at its ideal value of $c/a = \sqrt{8/3} \cong 1.633$, while for hex-ω this is a quantity that requires additional study and is discussed in detail below in Sec. IIIB. At low temperature, mechanical stability can be addressed by calculation of the quasi-harmonic phonon spectra, and we have calculated such spectra for selected phases over the volume and pressure ranges of interest here. More generally, we study the mechanical stability of individual phases through MGPT-MD simulation and appropriate diagnostic tools, principally calculation of the stress tensor. At high temperature, we simultaneously quantify the degree of vibrational anharmonicity in a given phase through calculation of the thermal energy.

A. Quasi-harmonic phonons

In agreement with first-principles DFT calculations at $T = 0$ [22,31], MGPT Ta is both mechanically and thermodynamically stable in the bcc phase over the present pressure range, which extends up to 420 GPa, with real quasi-harmonic phonons frequencies calculated throughout the Brillouin zone (BZ) at all volumes. The quality of the MGPT phonons obtained with the Ta6.8*x* potentials is indicated in Fig. 5, where calculated frequencies at the [100] and [110] zone boundaries, the *H* and *N* points in the BZ, respectively, are compared with DFT results [31] for a range of volumes and with experiment [43] at ambient conditions. There is good agreement among the MGPT, DFT, and experimental results, except for the anomalous transverse $T_2[110]$ phonon frequency, which is systematically underestimated with MGPT.

Similar quasi-harmonic MGPT phonon spectra have been calculated for the higher-energy fcc and hcp structures, and these results reveal imaginary phonon frequencies at all volumes considered. Representative results at a compressed volume of 88.65 a.u.,

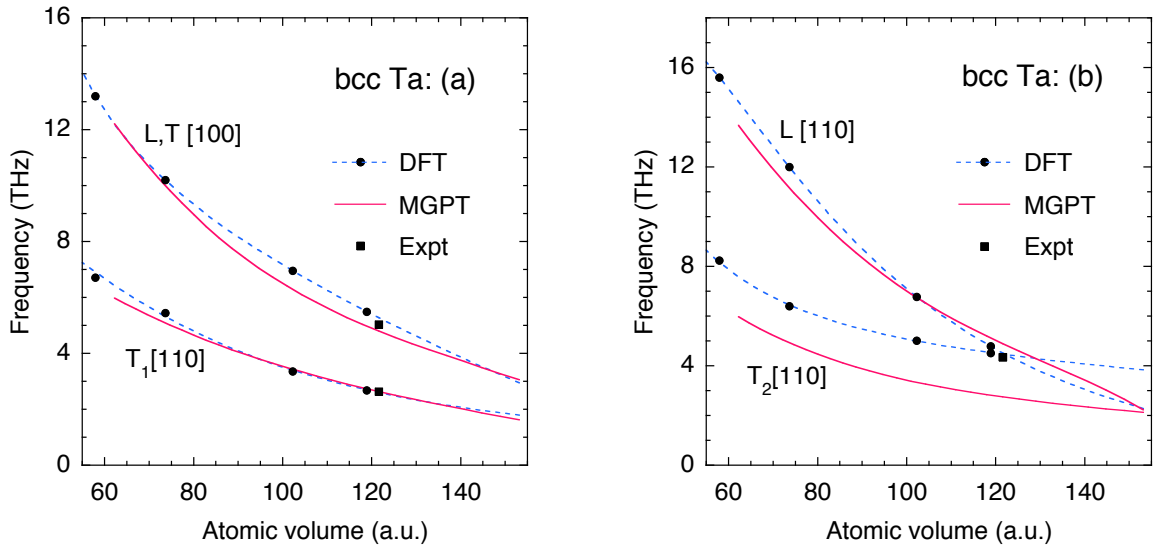

Fig. 5 Volume dependence of the longitudinal (L) and transverse (T, T_1, T_2) zone-boundary phonon frequencies in bcc Ta, as calculated from the present MGPT Ta6.8x potentials and as compared with previous DFT results [31] and with experiment [43]. (a) Degenerate H-point $L[100]$ and $T[100]$ phonons, and N point $T_1[110]$ phonon; (b) N-point $L[110]$ and $T_2[110]$ phonons.

corresponding to a $T = 0$ pressure of 109 GPa, are displayed in Fig. 6. In both the fcc and hcp structures, entire branches of phonon spectra are seen to be imaginary, indicating that these structures are indeed highly unstable mechanically at low temperature. This outcome also qualitatively agrees with DFT phonon calculations on these structures [22].

In the more complex A15 and hex-ω structures, with more than two atoms per primitive unit cell, we have alternately examined the low-temperature mechanical stability of these phases with MGPT-MD simulations. In contrast to the fcc and hcp structures, the lower-energy A15 structure, with eight atoms per primitive unit cell, was thereby found to be everywhere mechanically stable at 100 K. In this case, the mechanical stability of the structure was revealed both through calculated pair and angular distribution functions and through the calculated stress tensor, which displayed equal diagonal components and negligible off-diagonal components.

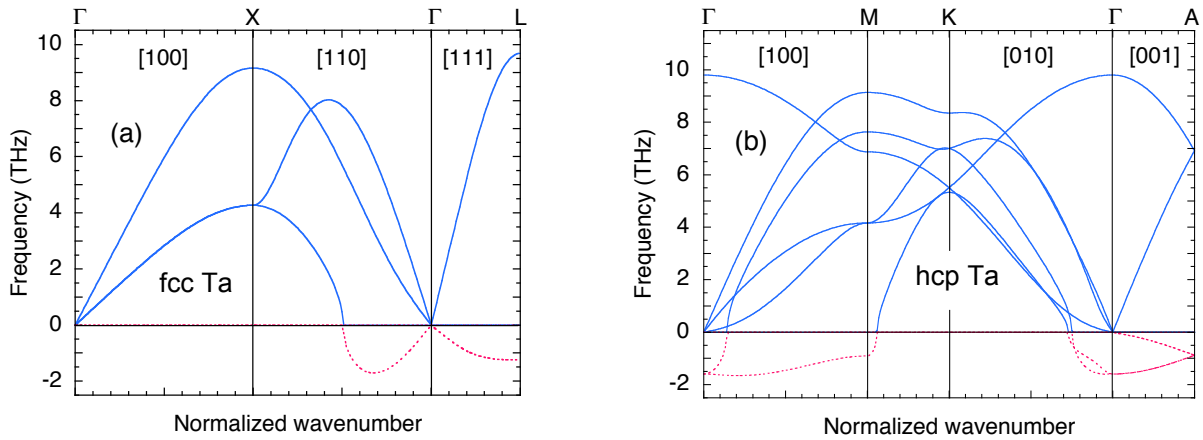

Fig. 6 Quasi-harmonic MGPT phonon spectra for mechanically unstable phases of Ta at low temperature, as calculated at a representative atomic volume of 88.65 a.u. with the present Ta6.8*x* potentials. Imaginary phonon frequencies (dashed lines) are plotted as negative numbers. (a) fcc structure; (b) ideal hcp structure.

B. Hexagonal omega phase

It is well known that the hex-ω phase appears in the equilibrium high-pressure phase diagrams of the group-IVB metals Ti, Zr, and Hf [44]. A variant of the hex-ω structure, the trigonal omega (trig-ω) structure, which contains a second internal parameter *z*, also appears in the phase diagrams of group-IVB alloys with other central transition metals, including the group-VB elements V, Nb and Ta. The ideal hex-ω structure with $c/a = \sqrt{3/8} \cong 0.6124$ is coincident with the trig-ω structure for $z = 0$, and from that point, the trig-ω structure provides a continuous structural path back to the bcc structure, which occurs for $z = 1/6$. In the Burakovsky *et al*. QMD simulations on Ta [22], it was found that if the material was initially placed in an ideal hex-ω phase, the structure would always relax back to bcc [45]. This behavior has been confirmed in our present MGPT-MD simulations, and suggests that the ideal hex-ω structure sits at an unstable saddle point in the c/a, z configuration space. In addition, at low temperature, where hex-ω is mechanically unstable in both QMD and MGPT-MD simulations, the electronic structure favors a smaller than ideal c/a ratio. This is demonstrated in Fig. 7, where $T = 0$ DFT and MGPT hex-ω – bcc total energy differences for predicted c/a ratios are compared.

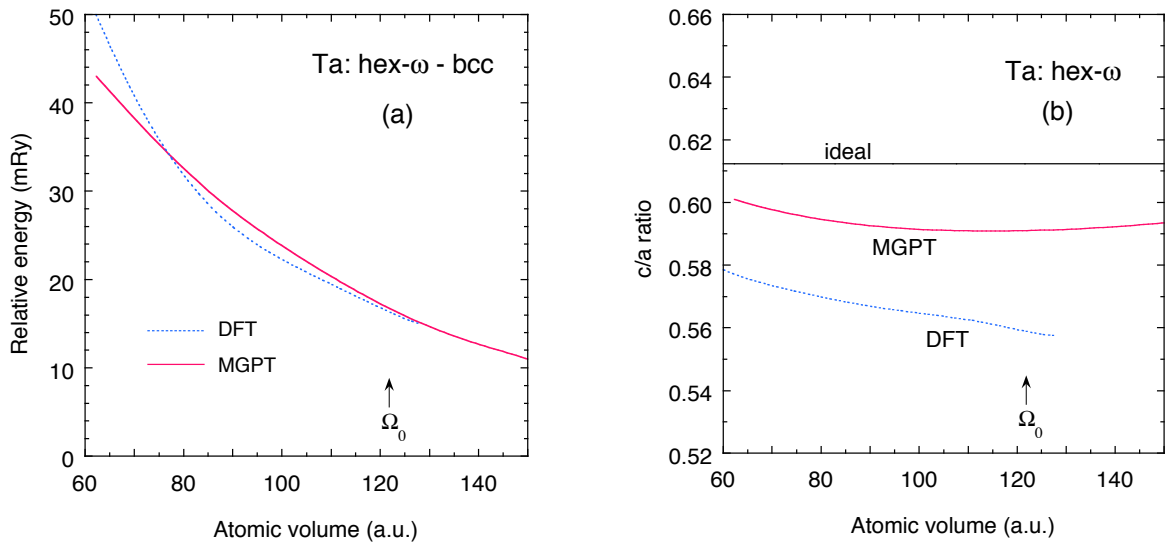

Fig. 7 Zero-temperature energetics of the hex-ω structure in Ta, as obtained from first-principles DFT electronic structure calculations [22] and from the present MGPT Ta6.8*x* interatomic potentials. (a) Hex-ω – bcc total-energy difference; (b) predicted hex-ω c/a ratio from total-energy minimization.

The DFT and MGPT results are in good agreement, but the MGPT c/a ratios are found to be ~ 0.02 or 3-4% higher than the DFT values. The $T=0$ DFT c/a values, which vary slowly from ~ 0.56 near ambient conditions to ~ 0.58 at high pressure, were used directly in the high-T,P fixed-cell QMD melt simulations for the hex-ω phase [22]. For the present MGPT-MD simulations, on the other hand, we have first studied the quality of high-T,P hex-ω mechanical stability achieved as a function of c/a.

At high-T,P conditions, there is, of course, no guarantee that the c/a ratio optimized on the basis of $T=0$ total-energy minimization (Fig. 7b) will produce a mechanically stable hex-ω structure. Ion-thermal stabilization of the hex-ω structure will impart a temperature dependence to c/a that cannot easily be determined without testing the mechanical stability with dynamical simulations. In molecular dynamics, this can be readily accomplished through *in situ* calculation of the stress tensor σ. A signature of mechanical stability in a dynamical system is equivalent diagonal, or normal, σ_{ii}

components (*i.e.*, $\sigma_{11} = \sigma_{22} = \sigma_{33}$), and negligible off-diagonal, or shear, σ_{ij} components. In our present MGPT-MD simulations, we quantify the first of these conditions with the parameter $\delta\sigma$, which describes the deviation of the normal stresses from the pressure:

$$\delta\sigma = \sqrt{(\sigma_{11}^2 + \sigma_{22}^2 + \sigma_{33}^2)/P^2 - 3} \ , \tag{9}$$

where pressure is related to the stress tensor through $P = -(\sigma_{11} + \sigma_{22} + \sigma_{33})/3$. The second condition can be represented by the deviation of the shear stresses from zero, but for hex-ω this measure is negligible for a large range of c/a at high temperature, leading to our consideration of $\delta\sigma$ as the primary measure of mechanical stability.

The volume-averaged mechanical stability parameter $\langle\delta\sigma\rangle_\Omega$ calculated for the hex-ω structure is shown in Fig. 8a as a function of c/a for high-T values ranging from 1000 to 5000 K. For each temperature considered, $\langle\delta\sigma\rangle_\Omega$ displays a large peak separating two distinct c/a regimes of low $\delta\sigma < 0.025$ and hence good mechanical stability: (i) near the ideal hex-ω value of 0.6124; and (ii) at lower values in the narrow range 0.51-0.53. The first regime corresponds to the conditions where the hex-ω structure has relaxed to bcc. Inspection of the radial distribution functions for c/a values to the right of the main peaks in $\langle\delta\sigma\rangle_\Omega$ suggests some mixture of the hex-ω and bcc structures has occurred in this regime, and that this mixture becomes all or mostly bcc at c/a = 0.6124. To the left of the main peaks, on the other hand, the material appears to have settled into a clear hex-ω structure with good mechanical stability.

To confirm this interpretation of Fig. 8a and to better characterize the structural behavior corresponding to the mechanically stable values of c/a, we have tracked the evolution of trig-ω z displacements for systems initially in a hex-ω $z = 0$ state with a given c/a ratio. The final calculated distribution of z displacements, denoted by $N(z)$, is shown in Fig. 8b for three values of c/a at the specific conditions $T = 5000$ K and $\Omega = 80$ a.u. At the ideal hex-ω c/a ratio, we see that $N(z)$ evolves three equally distributed and well-defined z parameters at $z = 0$ and $z = \pm 0.167$, signifying the presence of a trig-ω

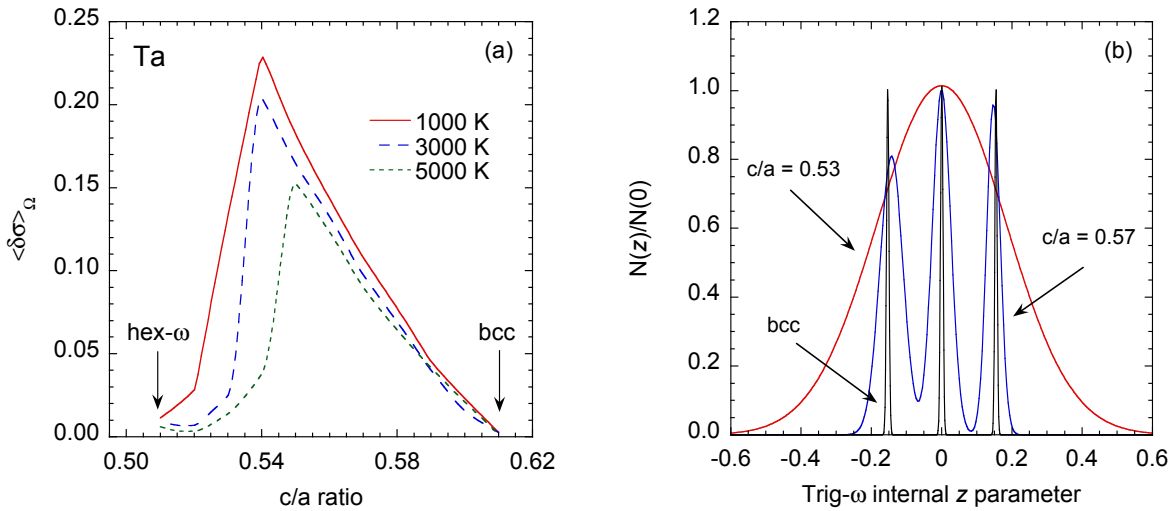

Fig. 8 (a) Volume-averaged mechanical stability parameter $\langle \delta\sigma \rangle_\Omega$ for the hex-ω phase of Ta, as calculated from MGPT Ta6.8*x* potentials using large $10 \times 10 \times 10$ computational cells. Here $\delta\sigma$ is averaged over the atomic volume Ω in the range 65-110 a.u. and is shown for temperatures 1000, 3000, and 5000 K. (b) Internal trig-ω z parameter as evolved from a hex-ω $z = 0$ initial state for c/a = 0.53, 0.57, and 0.6124. The distribution function $N(z)$ is evaluated at T = 5000 K and an atomic volume Ω = 80 a.u.

structure with $z = 0.167$ or, equivalently, bcc. At intermediate c/a values, where $\delta\sigma$ becomes large, the mechanical instability translates into an incomplete transformation into the bcc phase. This is indicated in Fig 8b by the $N(z)$ function at c/a = 0.57 displaying three broadened, more diffuse peaks that are unequally distributed, suggesting the presence of a mixture of hex-ω and bcc. Finally, the mechanically stable regime at low c/a, represented in Fig 8b by the c/a = 0.53 curve, results in $N(z)$ no longer exhibiting clearly defined z values but instead a completely diffuse distribution centered on $z = 0$. We interpret this behavior as the point at which the internal energy barriers to the hex-ω phase are fully overcome, enabling the mechanical stabilization of the structure. However, contrary to what might be expected for hex-ω, the diffuse z distribution implies that the calculated structure is probably a somewhat disordered variant of the ideal crystalline structure at this lower c/a ratio. Regardless, this state is

the most mechanically stable and characteristically hex-ω phase attainable that does not partially transform into the bcc phase.

For the present MGPT-MD studies of Ta polymorphism, we have used the above results to establish a good representative c/a value for a mechanically stable hex-ω phase over the expected high-T,P conditions that bound the hex-ω melt curve. As shown in Fig. 8a, the c/a ratio representing the onset of good mechanical stability for the hex-ω phase is somewhat dependent on temperature. Structures at the lower end of the c/a spectrum near 0.51 become fully stable at temperatures greater than 1000 K. However, as we expect the majority of the hex-ω melt curve to lie above 1000 K, a higher value of c/a = 0.53 provides the required stability at temperatures more representative of melt conditions, $T > 3000$ K. We therefore have used this latter ratio in all of the hex-ω MGPT-MD simulations performed in the remainder of this paper, except when comparing directly with the QMD simulations of Burakovsky *et al*. [22] in Sec IVB, where it is more appropriate to use a c/a value based on $T = 0$ total-energy minimization. In this regard, it is noteworthy that c/a = 0. 53 is significantly smaller than the $T = 0$ MGPT values indicated in Fig. 7b, which are in the range 0.59-0.60. We will comment further in Sec. IVB on the corresponding changes in melt behavior when using a $T = 0$ c/a ratio of 0.59 as opposed to a high-T value of 0.53.

C. High-temperature stress tensor for other candidate phases

We next consider the high-T,P mechanical stability of the remaining candidate polymorphic phases. As was shown in Fig. 6, the fcc and hcp structures have imaginary phonon modes, which imply mechanical instability at $T = 0$. To perform physically relevant melt simulations for these phases, we must first establish that they also attain good high-T,P mechanical stability. To do this we characterize the stress tensor in the same manner as above and consider the mechanical stability parameter $\delta\sigma$. It is now more convenient to perform a high-temperature average of $\delta\sigma$ than the volume average used above. The temperature-averaged mechanical stability parameter $\langle\delta\sigma\rangle_T$ as a function of atomic volume is displayed in Fig. 9 for the five phases considered in this

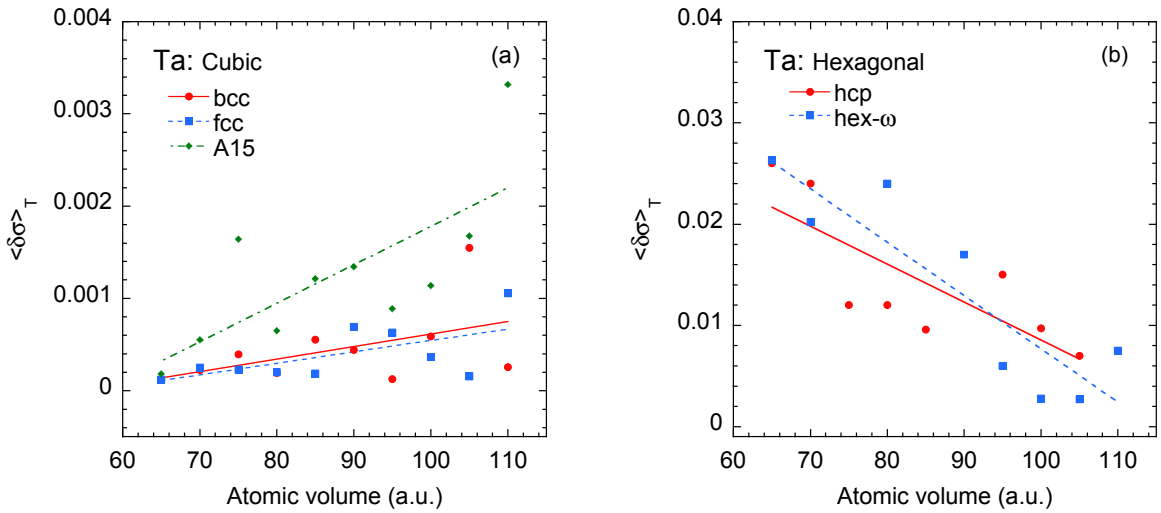

Fig. 9 Temperature-averaged mechanical stability parameter $\langle \delta\sigma \rangle_T$ for the candidate polymorphic phases of Ta, as calculated from MGPT Ta6.8*x* potentials using large $10 \times 10 \times 10$ computational cells. Here $\delta\sigma$ has been averaged over temperatures between 3000 K and the critical melt point T_c at each volume. (a) Cubic bcc, fcc, and A15 structures; (b) hexagonal hcp and hex-ω structures, with c/a ratios of 1.633 and 0.53, respectively.

work. Here the temperature average has been taken over the range $T_{\min} < T < T_c$, where $T_{\min} = 3000$ K and T_c is the volume-dependent critical melt point as defined in Fig. 4. The bcc, fcc, and A15 structures (Fig. 9a) all show a high degree of mechanical stability over the volume and temperature ranges considered, with $\langle \delta\sigma \rangle_T < 0.002$ except for one A15 point near 110 a.u. The hexagonal phases (Fig. 9b) show larger, but still small, mechanical instability that decreases with atomic volume. The small residual instability for the hexagonal phases is likely related to our choice of fixed c/a ratios, where realistically c/a should vary as a function of T and Ω. However, in comparison to the much higher level of mechanical instability displayed in Fig. 8 for the hex-ω structure with larger c/a, the magnitude of $\delta\sigma$ for the hexagonal phases treated in Fig. 9b is acceptably small, with $\langle \delta\sigma \rangle_T < 0.03$ for all volumes.

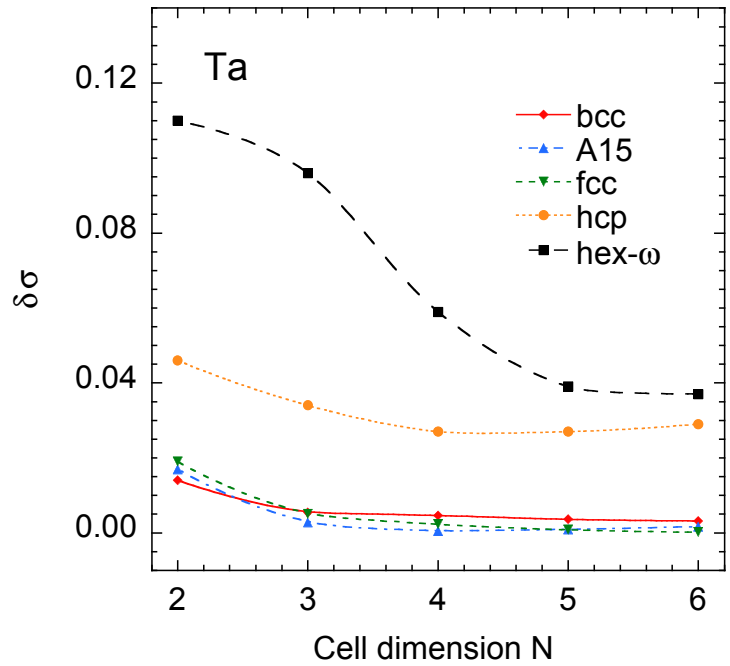

Fig. 10 Dependence of the mechanical stability parameter $\delta\sigma$ on cell dimension N for an $N \times N \times N$ simulation cell, as obtained for the five candidate polymorphic phases of Ta. The simulations have all been performed at $T = 5000$ K and an atomic volume of 80 a.u., with $c/a = 1.633$ for hcp and 0.53 for hex-ω, for system sizes ranging from $2 \times 2 \times 2$ to $6 \times 6 \times 6$.

An additional point of importance when considering melt behavior is the dependence of $\delta\sigma$ on the size of the periodic simulation cell. The size of the cell directly controls the available phonon modes and, as such, influences high-T properties that depend on phonon-phonon interactions, especially vibrational anharmonicity and its mediation of mechanical stability. Such an influence is apparent in Fig. 10, which shows the degree of mechanical stability achieved as a function of the size of the simulation cell at the representative conditions of $T = 5000$ K and $\Omega = 80$ a.u. As given in Fig. 10, the cell dimension N represents the effective number of unit cells along each of the three unit vectors defining the cell, such that the full simulation cell contains $N \times N \times N$ unit cells. We see that the mechanical stability of all phases is significantly decreased in small systems less than $4 \times 4 \times 4 = 64$ unit cells in size. While the cubic structures become fully mechanically stable when the system is composed of a minimum of 64 unit cells,

the hexagonal phases appear to require a larger size of at least $5 \times 5 \times 5 = 125$ unit cells to achieve their maximum stability. These limits correspond to 128 atoms for bcc, 256 atoms for fcc, 512 atoms for A15, 250 atoms for hcp and 375 atoms for hex-ω. This suggests that except for bcc, cell sizes of 250-500 atoms may be required to eliminate size effects. In any case, we can expect such size effects to influence the melt behavior derived from small simulation cells, and this possibility will be examined in detail in Sec. IVB below in the context of Z-method melting.

D. High-temperature anharmonicity

One may also address the degree of vibrational anharmonicity in a given phase and its size dependence more directly. The phonon-phonon interactions that stabilize phases with imaginary quasi-harmonic phonons can be characterized at high-T,P conditions by the apparent amount of anharmonicity displayed in appropriate thermodynamic functions. Specifically, we can define a simple but useful percentage measure of anharmonicity in a given phase, Q_{ah}, by the relation

$$Q_{\mathrm{ah}}(\Omega,T) = 100[1 - E_{\mathrm{th}}(\Omega,T)/3k_{\mathrm{B}}T] \ , \tag{10}$$

where $E_{\mathrm{th}} = E_{\mathrm{tot}} - E_0$ is the thermal energy of the system in that phase, with E_{tot} the total internal energy. In the quasi-harmonic limit at high temperature with $A_{\mathrm{el}} = E_{\mathrm{el}} = 0$, $E_{\mathrm{th}} \to 3k_{\mathrm{B}}T$ and $Q_{\mathrm{ah}} \to 0$. Figure 11a shows how Q_{ah} varies with atomic volume, as calculated from MGPT-MD simulations at a representative temperature $T = 5000\,\mathrm{K}$ for the five phases considered in this work. The bcc and A15 phases show only a minor degree of anharmonicity, ~ 0.1% and ~ 1-3% respectively, which in part reflects the low-T mechanical stability of these structures. On the other hand, the metastable fcc and hcp phases show a significant and similar degree of anharmonicity, ~ 4-9%, which increases with increasing atomic volume, with fcc slightly more anharmonic than hcp over the entire volume range. The hex-ω phase is by and large the most anharmonic of the phases considered here and is drastically influenced by the atomic volume. Over the selected atomic volume range, Q_{ah} for hex-ω varies from ~ 40% at high pressure to ~ 10% at low

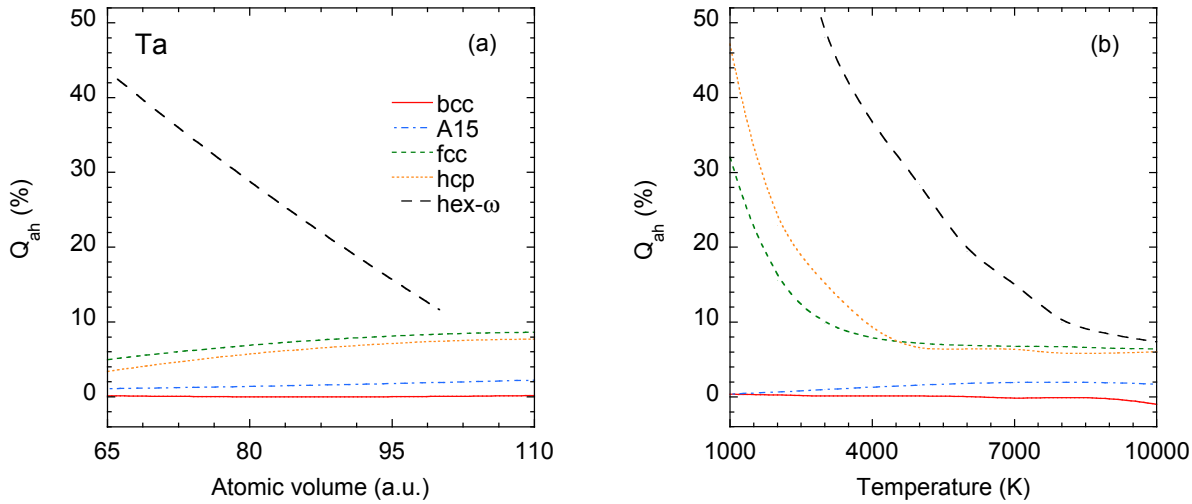

Fig. 11 Vibrational anharmonicity Q_{ah} of candidate polymorphic phases in Ta as a function of volume and temperature, as calculated from MGPT-MD simulations with the Ta6.8*x* potentials and large $10\times10\times10$ computational cells. The c/a ratios used for the hcp and hex-ω structures were 1.633 and 0.53, respectively. (a) Volume dependence for $T=5000$ K up to the low-pressure melt volume; (b) temperature dependence for atomic volume $\Omega=80$ a.u. up to and above melt.

pressure. Such high anharmonicity may be partially attributed to the fact, as previously noted, that the ideal hex-ω structure at $c/a=0.53$ undergoes some structural disorder in attaining its mechanical stability.

Figure 11b displays the corresponding temperature dependence of the vibrational anharmonicity at a representative atomic volume $\Omega=80$ a.u. For the bcc and A15 phases Q_{ah} remains small and nearly constant from 1000 to 10000 K, reflecting the mechanical stability of these phases at all temperatures. The anharmonicity Q_{ah} also remains nearly constant for the fcc and hcp phases above 4000 K, but rapidly increases below that point, while Q_{ah} rapidly increases for the hex-ω phase below about 8000 K. This behavior is consistent with greater structural rearrangement as the temperature decreases resulting in complete mechanical instability at $T=0$.

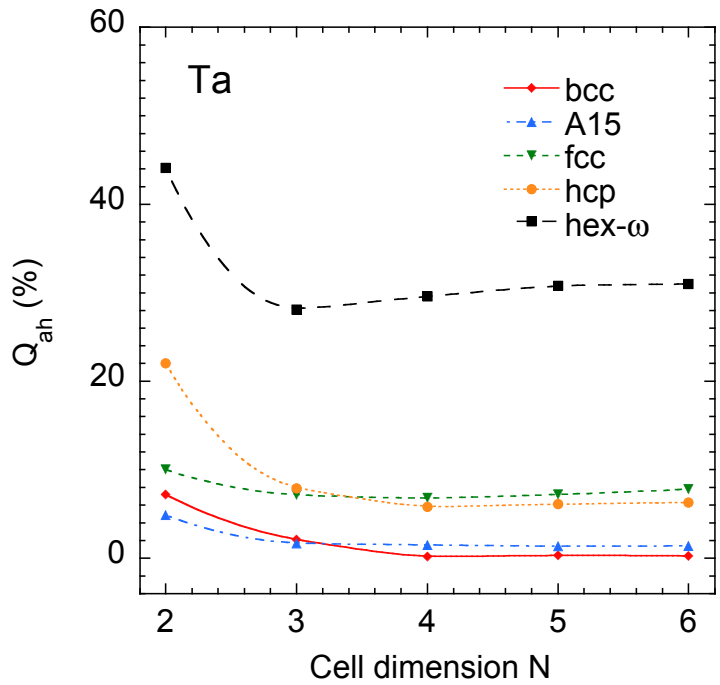

Fig. 12 Dependence of the vibrational anharmonicity Q_{ah} in Ta on size of the simulation cell for candidate polymorphic phases, as in Fig. 10. The calculations were performed at T = 5000 K and an atomic volume $\Omega = 80$ a.u., with $c/a = 1.633$ for hcp and 0.53 for hex-ω, for system sizes ranging from $2\times2\times2$ to $6\times6\times6$.

In a manner similar to Fig. 10, one can also calculate the variation in the vibrational anharmonicity Q_{ah} as a function of the size of the periodic simulation cell for each of the candidate polymorphic phases. We have done this here for the representative conditions $T = 5000$ K and $\Omega = 80$ a.u. and the results are displayed in Fig. 12. As might be expected, trends similar to those in the behavior of mechanical stability $\delta\sigma$ are reflected in Q_{ah}. Specifically, the hcp and hex-ω structures are significantly influenced at sizes less than $4\times4\times4 = 64$ unit cells, while the bcc, fcc, and A15 phases show a smaller influence and well converged behavior by 64 unit cells. In contrast, the hex-ω phase requires at least $5\times5\times5 = 125$ unit cells for similar convergence. Thus the size effects displayed in Fig. 10 for $\delta\sigma$ and in Fig. 12 for Q_{ah} are indeed very consistent.

IV. MELT RESULTS for CANDIDATE HIGH-T,P SOLID PHASES

In this section we discuss the high-T,P melt behavior of bcc, A15, fcc, hcp, and hex-ω Ta, as obtained with both two-phase and Z-method MGPT-MD simulations. In each case, an important consideration is to characterize the effects of the simulation cell size on the resulting melt behavior. There are in fact two main size effects. The first is the statistical fluctuation of individual melts points, which generally grows larger as the cell size is decreased. As we have implemented the two-phase and Z methods, such statistical fluctuations are more problematic for the former method than the latter. Although for bcc metals, our two-phase melt method has been successfully used with as few as 256 atoms in $8\times4\times4$ computational cells, including both MGPT-MD and QMD simulations [25], this has proven more difficult for the non-bcc Ta phases of interest here. For the present two-phase melt simulations, we find the desirable minimum cell size is $20\times10\times10$, corresponding to 4000-16000 atoms for the non-bcc phases, which is already in the large-cell limit. Consequently, the second and more important melt size effect, the net movement of the melt curve up or down in temperature, is more readily studied with the Z method. By its very construction, the Z-method allows the use of much smaller simulation cells, down to $2\times2\times2$, and with it we test the implications of the size-dependent stress tensor and anharmonicity discussed above in Sec. III on melt behavior. As our primary goal is to address high-T,P polymorphism in Ta and determine its implications for high-pressure melting, we compare the large-cell melt behavior of the two-phase simulations and the Z methods, noting the systematic differences between the two methods and their consequences for the predicted phase diagram.

A. Two-phase melt curves for large cells

Before discussing the relative stability of our candidate phases predicted from large-cell two-phase melt calculations, we briefly elaborate on how size-related effects influence the melt behavior with this method. Although we had initially attempted two-phase calculations with smaller $8\times4\times4$ simulation cells, the resulting rapid convergence and fluctuation of the $\mathrm{O}_6(t)$ order parameter was difficult to accurately analyze, especially for the non-bcc phases. To sufficiently damp such fluctuations for all phases, we have

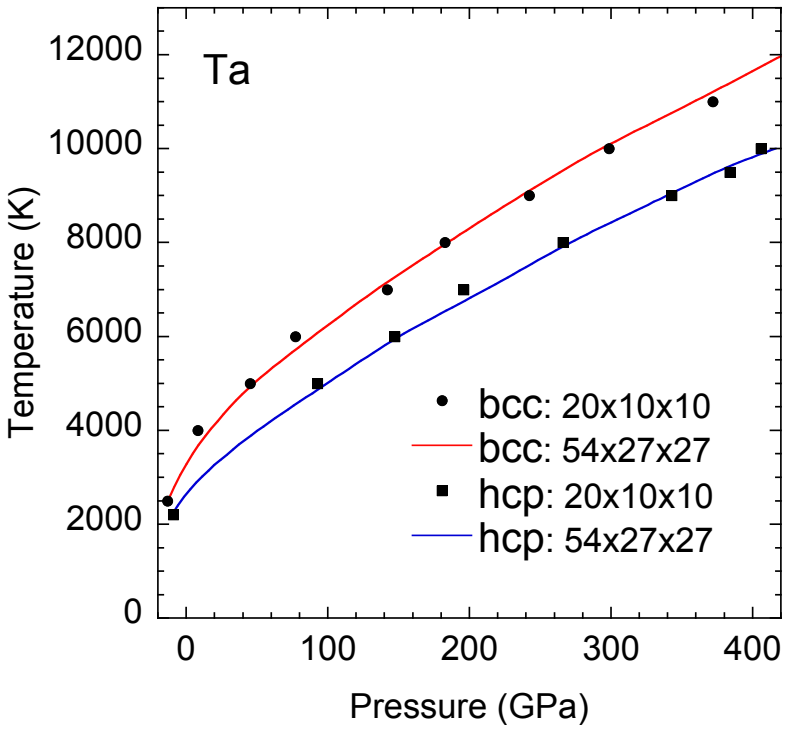

Fig. 13 Large-cell smoothing of the melt curve in two-phase MGPT-MD simulations for bcc and hcp Ta, as calculated with the Ta6.8*x* potentials.

found that system sizes no smaller than $20\times10\times10$ are required. To fully smooth the melt curves, we have also performed two-phase simulations with much larger cells, with ~ 80000 atoms for each phase. This requires simulation cells of $54\times27\times27$ for bcc and hcp, $46\times23\times23$ for hex-ω, $42\times21\times21$ for fcc, and $34\times17\times17$ for A15. The resultant smoothing of the melt curve is illustrated in Fig. 13 for bcc and hcp Ta. Here the increased cell size does not qualitatively change the melt behavior, but the larger cells improve the overall quality of the melt curve by removing the small fluctuations present in the $20\times10\times10$ results. For this reason, all the remaining two-phase simulations discussed below refer to the larger cells with ~ 80000 atoms.

The melt curves calculated from our large-cell two-phase simulations for all five of our candidate phases are displayed in Fig. 14. The most significant feature of these results is that the bcc phase has the highest melt curve and hence is predicted to be the most stable of the solid phases considered across the entire simulated pressure range, -11 to 420 GPa.

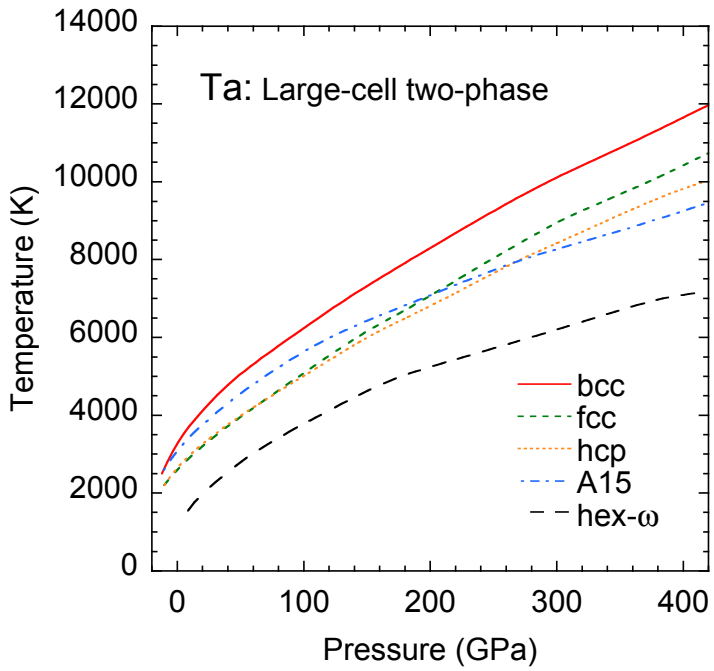

Fig. 14 Melt curves calculated from large-cell, ~ 80000-atom, two-phase MGPT-MD simulations with the Ta6.8*x* potentials for bcc, fcc, hcp, A15, and hex-ω Ta over a pressure range of -11 to 420 GPa. The c/a ratios used for the hcp and hex-ω structures were 1.633 and 0.53, respectively.

In contrast, the hex-ω phase with $c/a = 0.53$ has the lowest calculated melt curve and hence is the least stable of all the considered phases, with melt temperatures 1000-2500 K below those of the next most stable phase, hcp. This may seem to be a surprising result in light of the recent QMD studies on Ta [22], which predict a thermodynamically stable hex-ω phase above 70 GPa, but the MGPT and QMD results can be readily reconciled in terms of size effects and choice of c/a ratio, as discussed in the next section (Sec. IVB) on Z-method melting.

Collectively, the Ta melt curves presented in Fig. 14 represent our most accurate MGPT-MD results and serve here as a baseline with which to compare large-cell Z-method melt results in Sec. IVC below. Several specific quantitative aspects of these results should also be mentioned. First, the bcc melt curve in Fig. 14 is the same as the two-phase result plotted in Fig. 3, so by comparing Figs. 2 and 3 we infer that the two-phase bcc melt curve is indeed in good agreement with experiment. The calculated bcc melt temperature

and slope, T_{m} and dT_{m}/dP, at $P=0$ are 3222 K and 51 K/GPa, respectively – in good agreement with experimental measurements of 3270 K [7,11] and ~ 59 K/GPa [11] and also in accord with other recent theoretical results [18-20]. The calculated T_{m} at the observed shock melt pressure of 295 GPa [15] is 10000 K and close to the value recently measured by pyrometry of ~ 9700 K. As a further point of interest in Fig. 14, the A15 melt curve is seen to approach the bcc melt curve from below at low pressure with the two crossing near $P=-11$ GPa and $T_m=2500$ K, while at higher pressure the A15 curve moves well below the bcc curve. This is consistent both with the observed metastability of the A15 phase at ambient pressure [1] and with previous MGPT-MD studies [2] in which rapid solidification of liquid Ta yielded evidence of both bcc and A15 at low *P* but only bcc at high *P*. Finally, the fcc and hcp phases have almost the same melt curves at low pressure, but begin to separate above 100 GPa to slightly favor the fcc phase. By fitting a Simon functional form to the melt curves of these phases, we have determined that the fcc and hcp curves cross the A15 melt curve at 204 GPa and 267 GPa, respectively.

The relationship between the degree of vibrational anharmonicity, Fig. 11, and the relative stability of the candidate phases as given by the two-phase simulations, Fig. 14, also warrants some additional discussion. Strictly speaking, there is no necessary or established relationship between anharmonicity and relative melt behavior, but we note that increased anharmonicity appears to signify a trend in the melt temperature to higher pressure in Ta, at least up to about $T_{\mathrm{m}}=7000$ K. For instance, by considering $T_{\mathrm{m}}=5000$ K in Fig. 14, one sees that $P_m^{bcc}<P_m^{A15}<P_m^{fcc}\sim P_m^{hcp}<P_m^{hex-\omega}$, with bcc and hex-ω being the most and least stable phases, respectively. This closely reflects the degree of anharmonicity noted at $T=5000$ K in Fig. 11, bcc having the smallest $Q_{ah}\cong 0.1\%$ and hex-ω having the largest Q_{ah} ranging from 10% to 40%. Such a trend does not necessarily yield the specific details of the melt curves that can be observed from two-phase simulations, but it suggests that anharmonicity might be a useful diagnostic tool for analyzing melt behavior at lower T_{m} and P_m.

B. Z-method melt curves for small and large cells

An attractive aspect of the Z method is its applicability to small simulations cells – a feature that allows the method to be extended to potentially more accurate, but much more computationally expensive, quantum simulation techniques like QMD. However, in Z-method QMD simulations, size-independent melt behavior is not guaranteed, and, considering the significant effect size has on mechanical stability (Fig. 10) and anharmonicity (Fig. 12) in the present MGPT-MD simulations, it is reasonable to expect some size-related influence on the melt curves. We have tested this supposition here by performing Z-method MGPT-MD simulations with both small and large simulation cells for our candidate phases. The small cells are composed of $3\times3\times3$ unit cells (54-216 atoms), and the large cell systems have $10\times10\times10$ unit cells (2000-8000 atoms). Except for the A15 structure with 216 atoms, the small cells are comparable to those used in the recent QMD simulations on Ta [22] and Mo [24]. Though the large cells are smaller than those we used in the two-phase simulations, we have tested specific melt points with cell sizes up to $20\times20\times20$ and found no qualitative difference in the resulting melt temperatures, as was similarly noted in the original Z-method MD simulations with empirical potentials [34]. Additionally, to eliminate the possibility of overestimations of T_c and T_m in our implementation of the Z method (Fig. 4), we have determined that 20 ps of equilibration is sufficient to allow systems at their critical melting point to relax into liquid. We have used this equilibration time in all of the following Z-method MGPT-MD melt simulations discussed below.

Figure 15 shows the results of our small- and large-cell Z-method MGPT-MD melt simulations for our five candidate polymorphic phases. The melt curves for the cubic structures are seen to be only slightly altered by size effects, with the bcc and A15 melt curves nearly the same and almost unchanged between the small-cell and large-cell results, while the fcc melt curve is modestly lowered with respect to the other two in the large-cell calculations. The impact of cell size on the hexagonal structures, on the other hand, is quite dramatic. From the small-cell melt curves displayed in Fig. 15a, one sees that the hcp and hex-ω phases are by far the most favorable structures, having melt temperatures thousands of degrees higher than those of the cubic structures.

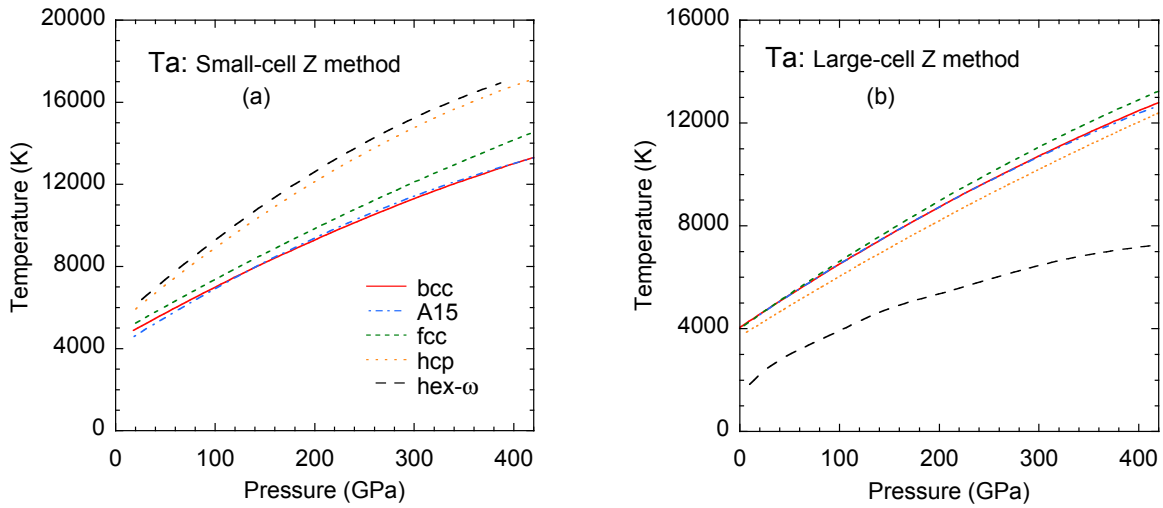

Fig. 15 Size dependence of the melt behavior, as obtained from the present Z-method MGPT-MD simulations for candidate phases of Ta using the Ta6.8*x* potentials. The c/a ratios used for the hcp and hex-ω structures were 1.633 and 0.53, respectively. (a) Small-cell $3\times3\times3$ melt curves; (b) large-cell $10\times10\times10$ melt curves.

Conversely, in the large-cell results displayed in Fig. 15b, the hcp and hex-ω melt curve have moved below those of the cubic structures, with hcp being slightly less stable than bcc and A15, and hex-ω being by far the least stable phase with melt temperatures now many thousands of degrees lower than the other phases, in qualitative agreement with the two-phase hex-ω melt curve in Fig. 14. This striking behavior is likely the result of the significant effects of cell size on mechanical stability and anharmonicity for the hexagonal phases, as shown in Figs. 10 and 12.

Several additional melting features revealed from the present Z-method simulations should also be mentioned. The nearly identical melt behavior of the bcc and A15 structures is qualitatively the same as obtained by Burakovsky *et al.* in small-cell QMD Z-melt simulations on Ta [22]. From the large-cell results in Fig. 15b, one further sees that at low-pressure below about 50 GPa the bcc and A15 phases are the most stable of the five phases considered, in qualitative agreement with the large-cell two-phase simulations in Fig. 14. As the pressure is increased, however, and in contrast to two-phase simulations, the fcc melt curve crosses above the bcc/A15 melt curve above 50

GPa and becomes the most stable phase at high pressure. The behavior of the bcc, A15 and fcc melt curves is also qualitatively similar to the previous Z-method melt results obtained with the Ta4 MGPT potentials [22]. In addition, the position of the large-cell hcp melt curve below that of bcc across the entire pressure range to 420 GPa in Fig. 15b is in qualitative agreement with the large-cell two-phase results in Fig. 14, as well as with the small-cell QMD simulations in Ref. [22]. In contrast to the QMD simulations, however, the present small-cell hcp melt curve lies above rather than below the bcc melt curve.

Regarding the present Z-method hex-ω melt results in Fig. 15, two further points should be made. First, there is significant quantitative sensitivity in the magnitude of the size effect to the c/a ratio, and this is an important consideration when comparing MGPT-MD and QMD melt curves, as we do below. The results shown in Fig. 15 are calculated for $c/a = 0.53$. For larger values of c/a, the small-cell hex-ω melt curve is lowered toward the bcc melt curve, while the large-cell hex-ω curve is raised toward the bcc curve, so the magnitude of the size effect is reduced, but it still remains substantial. The second point to mention is that the energy barrier between hex-ω and liquid Ta is quite low, resulting in very small values of $T_c - T_m$ in the Z method. For the other phases considered, this difference is typically ~ 2000 K, while for hex-ω the difference is more like ~ 200 K. This suggests that, while mechanically stable, the hex-ω phase is only slightly more favorable than the super-cooled liquid.

The large size effects found for the hexagonal phases have clear implications for small-cell applications of the Z-method in QMD, and in particular for the recent prediction of a stable high-pressure hex-ω phase in Ta [22]. While QMD provides excellent DFT quantum mechanics to establish forces for the molecular dynamics, the validity of the statistics produced from such a simulation with a small number of atoms can be questioned if size begins to influence structural phase stability through anharmonicity and mechanical stability. In Fig. 16 we attempt to make a valid comparison between MGPT-MD and QMD predictions of hex-ω and bcc melting, with the hex-ω c/a ratios used in each method established by $T = 0$ energy minimization, as in Fig. 7b. The QMD hex-ω

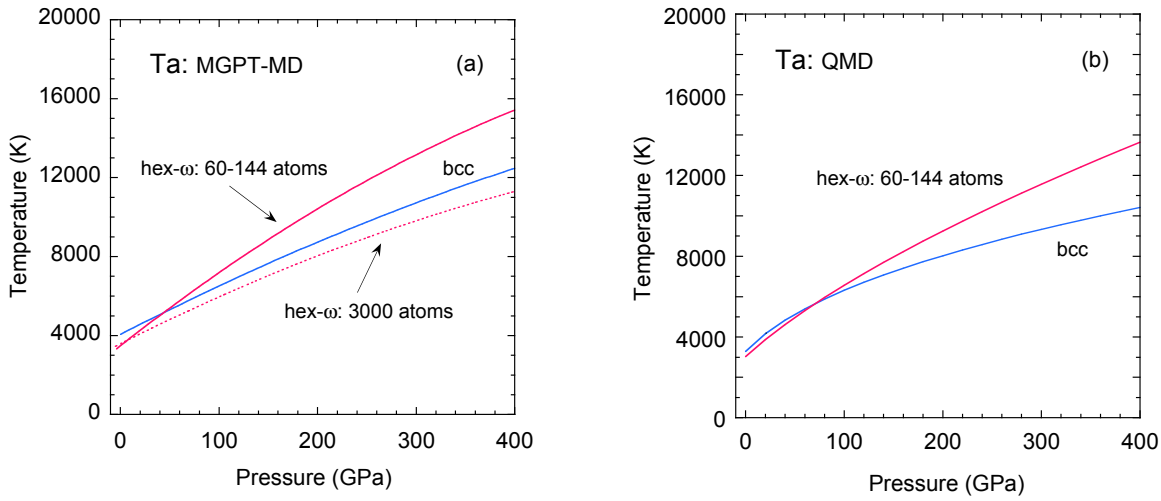

Fig. 16 Comparison of MGPT-MD and QMD melt curves for hex-ω and bcc Ta, as obtained with the Z method using hex-ω c/a ratios determined by respective total-energy minimization at $T=0$. (a) MGPT-MD simulation using the Ta6.8*x* potentials with $c/a=0.59$; (b) QMD simulation [22] with $c/a=0.56-0.58$.

melt curve shown in Fig. 16b is a fit to four Z-melt simulations carried out with small cells ranging from 60 to 144 atoms in size [46]. To make comparison with the QMD result, we performed both small-cell ($3\times3\times3$, 81 atom) and large-cell ($10\times10\times10$, 3000 atom) Z-melt simulations for the hex-ω phase with MGPT-MD, using $c/a=0.59$, as inferred from Fig. 7b. We performed additional small-cell hex-ω Z-melt simulations for 60 and 144 atoms to confirm that within this small size range the melt curves are qualitatively similar. The small-cell MGPT-MD and QMD hex-ω melt curves displayed in Fig. 16 are very consistent with each other qualitatively and quantitatively, with both melt curves crossing above the bcc melt curve below 100 GPa. Our large-cell MGPT-MD calculation in Fig. 15a shows, however, that size effects will indeed push the hex-ω melt curve entirely below the bcc curve. We expect that a similar size effect will be present in QMD, but that clearly requires independent verification. Although 3000-atom QMD Z-melt calculations are probably not feasible, it might be possible to do such simulations in the 250-500 atom range to investigate this issue further.

C. Two-phase vs. Z-method melt for large cells

Our discussion of Ta melt behavior to this point has focused on understanding the cell-size influence on the melt curves for candidate polymorphic phases, as obtained with the Z method, and calculating with both the two phase and Z methods the large-cell limits of melt for these phases, limits which are relevant to the high-T,P phase diagram in this metal. We now discuss the remaining differences between the large-cell melt curves of each method. As has been indicated, we believe that the melt curves obtained here from the large-cell two-phase simulations are an accurate reflection of the true equilibrium thermodynamics for MGPT Ta. This is supported in the case of bcc melt by close agreement with the free-energy determined melt curve (Fig. 3), as well as by good agreement with experiment (Figs. 2 and 3; Sec. IVA). The Z-method, on the other hand, is based on the conjectural assumption that for constant volume the solid at its critical melt point T_c has the same internal energy as the liquid at the equilibrium melt point T_m. Although in previous test cases [22,34] this assumption has been confirmed for ordinary stable phases through comparisons with the two-phase method, the reliability of this relationship has not been well established in metastable phases with significant vibrational anharmonicity present, especially elastically soft high-temperature phases that are only mechanically stabilized by that anharmonicity. Moreover, as we have already shown in Fig. 3, even for stable bcc Ta the MGPT-MD melt curve obtained with the Z method is actually just a close upper bound to that obtained by the two-phase method.

Figure 17 compares the large-cell melt curves as calculated with the two-phase and Z methods for the remaining non-bcc phases in Ta. As in the case of the bcc phase, the Z-method is seen to provide only an upper bound to the melting behavior when compared to the two-phase results for the fcc, A15, hcp and hex-ω phases. The magnitude of the apparent Z-method error is, however, much larger and on the order of 1000-3000 K, or 25-35%, for the fcc, A15, and hcp phases. The hex-ω phase, on the other hand, as shown in Fig. 17b, has a Z-melt curve within ~ 200 K of the two-phase result, so that its melt curve is comparable in accuracy to that of the bcc phase. The upward biasing of T_m with the Z method is especially significant for the fcc phase because, as previously shown in

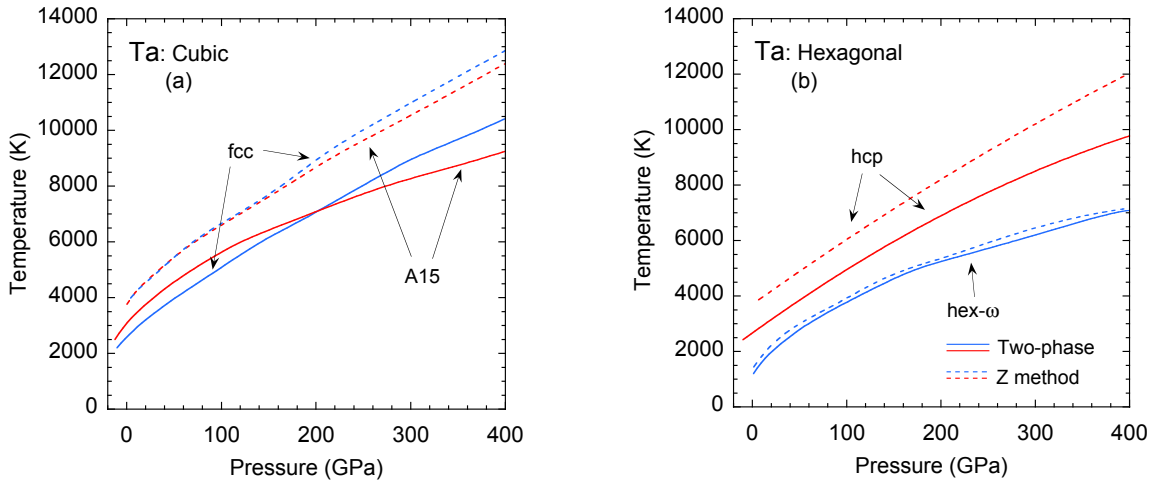

Fig. 17 Comparison of large-cell two-phase (solid lines) and Z-method (dashed lines) MGPT-MD melt curves for Ta as calculated from the Ta6.8*x* potentials. (a) Cubic structures: fcc and A15; (b) hexagonal structures: hcp and hex-ω, with $c/a = 1.633$ and 0.53, respectively.

Fig. 15b, it raises the fcc melt curve above that of bcc, leading to an incorrect prediction of a stable fcc phase at high pressure. Similarly, the flat melt profile of the A15 phase at high pressure as obtained by the two-phase simulations is largely absent in the Z-method result – instead the A15 and bcc phases have practically identical melt curves. Although the Z-melt curve for the hcp phase shows significant increases in melt temperature when compared to the two-phase result, the hcp melt curve remains entirely below that of bcc in both methods. Finally, the close similarity of the hex-ω melt curves from the two methods is striking, but perhaps it is not entirely surprising given the small energetic difference between hex-ω and liquid Ta.

The greater question raised by the comparisons shown in Figs. 3 and 17 is what role vibrational anharmonicity plays in the differences observed between Z-method and two-phase melt curves. The phases with both the smallest (bcc) and the largest (hex-ω) calculated anharmonicity yield the closest agreement between the two methods, while phases that display an intermediate degree of anharmonicity (A15, hcp, and fcc) produce

the largest differences. At the same time, and as previously noted in small-cell Z-method simulations for hex-ω, large increases in anharmonicity can result in exceptionally large increases in melt temperature. It may be that in the large-cell limit for hex-ω, the strong tendency of anharmonicity to push the Z-melt curve higher in temperature is offset by the small energetic barrier to melt, in which case the close agreement between the two-phase and Z methods for hex-ω in Fig. 17b may be somewhat fortuitous. But regardless, our results suggest that the Z-melt curve is always an upper bound, so that the energy required to induce homogeneous melting at T_c is generally larger than the internal energy increase from the solid to the liquid at T_m. Consequently, the relationship between T_c and T_m is likely more complex than Eq. (8) and possibly involves a number of other factors, including the degree of vibrational anharmonicity present and the size of the energetic barrier to melt.

V. DISCUSSION: IMPLICATIONS for HIGH-PRESSURE PHASE DIAGRAM

We have presented here an extensive study of polymorphism and melt in high-pressure Ta using quantum-based MGPT-MD simulations with new Ta6.8*x* interatomic potentials. This study has focused on candidate bcc, A15, fcc, hcp, and hex-ω phases for the high-T,P phase diagram to 420 GPa, examining the mechanical and relative thermodynamic stability of these phases for both small and large computational cells. The MGPT Ta6.8*x* potentials accurately capture the $T=0$ energetics of these phases, as previously established from first-principles DFT calculations [22,31], including a highly stable bcc ground state, a mechanically stable and competitive A15 structure at low pressure, and higher-energy, mechanically unstable fcc, hcp, and hex-ω structures with imaginary phonon frequencies. At high temperature, MGPT-MD simulations demonstrate that the fcc, hcp, and hex-ω structures are mechanically stabilized by large, but size-dependent, anharmonic vibrational effects. In the case of the hex-ω structure, the quality of the mechanical stability achieved is also found to be a sensitive function of c/a ratio, with good mechanical stability obtained in the range 0.51-0.53. For higher c/a values, the hex-ω phase partially transforms to bcc and only appears as a mixture with that structure, transforming completely to bcc at the ideal $c/a=0.6124$.

Two-phase and Z-method melting techniques have been used in establishing relative phase stability and its size dependence at high-T,P conditions. In the large-cell limit, the two-phase method provides accurate equilibrium thermodynamics and absolute MGPT-MD melt curves for all of the candidate solid phases. The bcc phase produces the highest melt temperatures at all pressures considered and hence is the lone predicted stable solid phase in the Ta phase diagram to 420 GPa. The two-phase bcc melt curve is also in good agreement with dynamic experimental data, as well as in close agreement with the MGPT melt curve calculated from bcc and liquid free energies. At the other extreme, the hex-ω phase with $c/a=0.53$ produces the lowest melt temperatures of the structures considered and is only slightly more stable thermodynamically than the super-cooled liquid. The melt curves for the remaining metastable A15, fcc, and hcp phases are calculated to be within 2000 K of the bcc melt curve, and these phases might be

accessible under certain experimental conditions. In particular, the A15 and bcc melt curves approach each other at low pressure, consistent with the observed solidification of a metastable A15 phase out of the melt [1].

In contrast to the two-phase method, we find that the Z method produces only an upper bound to the melt behavior in the large-cell limit. For the bcc and hex-ω phases the Z-melt curves are within 5% of the corresponding two-phase results, but for the A15, fcc, and hcp phases the Z-melt curves are 25-35% higher in temperature. This leads to the incorrect prediction of a stable fcc solid phase at high pressure with the Z method. Nonetheless, the Z method has allowed us to examine carefully size effects on the melt behavior in Ta with MGPT-MD simulations. We find that such size effects are small for bcc and A15, modest for fcc, but quite large for the hexagonal hcp and hex-ω structures, with the melt curves for the latter phases lying above that of bcc for small simulation cells with less that 150 atoms, but with these curves being pushed below bcc in the large-cell limit. We have further shown that the size effects on the melt curve are driven by and closely correlated with similar size effects on vibrational anharmonicity, as measured by the thermal energy, and on mechanical stability, as measured by the stress tensor. We conclude that for the non-bcc metastable phases in Ta, one requires simulation cells of at least 250-500 atoms to be safely free of such size effects.

Additional Z-melt MGPT-MD simulations for hex-ω with the c/a ratio determined by $T=0$ energy minimization have also allowed us to compare our results directly with the small-cell QMD prediction [22] of a stable high-pressure hex-ω phase in Ta. Under the assumed conditions, our small-cell MGPT-MD results confirm the QMD prediction, with the hex-ω melt curve crossing above that of bcc below 100 GPa. However, when the same calculation is repeated in the large-cell limit, the hex-ω melt curve is again pushed entirely below the bcc melt curve. Whether or not this would also be the case in QMD requires much larger simulations than have currently been attempted for bcc transition metals [22,24] to answer, but both two-phase and Z-melt QMD simulations in the 250-500 atom range for Ta should be feasible.

In any future theoretical investigations of high-T,P polymorphism in transition metals, it would be desirable to entertain other considerations as well. One such consideration is the use of variable-shaped simulation cells as opposed to the fixed-shaped cells that have been used heretofore. The use of a variable-shaped cell is clearly more computationally challenging, but it would allow the full relaxation of structures with internal degrees of freedom such as hex-ω, so that, for example, the simulation could decide the optimum c/a ratio in any environment and not have that choice imposed as an external constraint. This would also allow the possibility of treating complex structures with more than two atoms per primitive cell. Another possible consideration in this regard is the use of genetic algorithms or similar techniques to generate additional candidate structures. In the case of Mo, for example, the use of genetic algorithms recently uncovered several complex structures with $T = 0$ energies much closer to that of bcc than is the case for the fcc, hcp or hex-ω structures [47].

Finally, there is clearly a need for more and better experimental data, both static and dynamic, to constrain the phase diagram at high-T,P conditions in bcc transition metals. While the existing sound velocity data along the shock Hugoniot in Mo [17] and Ta [15,22] suggest possible solid-solid phase transitions prior to melt, this is far from a certain conclusion. In both cases, for example, the removal of a single point from the data set would argue against such a transition. As a result, there is currently an ongoing experimental effort to repeat these measurements more accurately [48]. The correct interpretation of the flat DAC melting curves in bcc metals [7-9] is also an open question. The disappearance of bcc x-ray diffraction lines, which was interpreted as melting in these experiments, could instead be the result of some other phenomena, including unwanted chemical reactions [28] or the onset of rapid recrystallization associated with a solid-solid phase transition [22]. To date, however, no other solid structure than bcc has been identified by x-ray diffraction in high-T,P DAC experiments on these materials. The use of x-ray diffraction in dynamic high-T,P investigations of the phase diagram is also an interesting possibility for the future. In laser-driven shock experiments on iron [49], for example, nanosecond x-ray diffraction has been used to make direct observation of the well-known bcc to hcp phase transition at 13 GPa.

ACKNOWLEDGMENTS

This work was performed under the auspices of the U.S. Department of Energy by Lawrence Livermore National Laboratory under Contract No. DE-AC52-07NA27344. J.B.H. acknowledges support as a summer student at LLNL in 2011 from DOE SciDAC Grant No. DE-FC02-06ER25788, during which time this work was begun. The authors wish to thank L. Burakovsky for useful discussions and information about the QMD Ta simulations reported in Ref. 22. They also thank A. S. Mikhaylushkin for numerical tables of the $T = 0$ DFT structural data reported in Ref. 22, which were used in making Fig. 7.

REFERENCES

[1] L. Cortella, B. Vinet, P. J. Desre, A. Pasturel, A. T. Paxton, and M. van Schilfgaarde, Phys. Rev. Lett. **70**, 1469 (1993).

[2] J. A. Moriarty, J. F. Belak, R. E. Rudd, P. Söderlind, F. H. Streitz, and L. H. Yang, J. Phys.: Condens. Matter **14**, 2825 (2002).

[3] W. R. Morcom, W. L. Worrell, H. G. Sell, and H. I. Kaplan, Metall. Trans. **5**, 155 (1974).

[4] F. H. Streitz and J. A. Moriarty, LLNL Report No. UCRL-JC-148950, 2002; F. H. Streitz, J. N. Glosli, and M. V. Patel, Phys. Rev. Lett. **96**, 225701 (2006).

[5] J. A. Moriarty, Phys. Rev. B **42**, 1609 (1990); **49**, 12431 (1994).

[6] J. A. Moriarty, L. X. Benedict, J. N. Glosli, R. Q. Hood, D. A. Orlikowski, M. V. Patel, P. Söderlind, F. H. Streitz, M. Tang, and L. H. Yang, J. Mater. Res. **21**, 563 (2006).

[7] D. Errandonea, B. Schwager, R. Ditz, C Gessmann, R. Boehler, and M. Ross, Phys. Rev. B **63**, 132104 (2001).

[8] D. Errandonea, M. Somayazulu, D. Häusermann, and H. K. Mao, J. Phys.: Condens. Matter **15**, 7635 (2003).

[9] D. Santamría-Perez, M. Ross, D. Errandonea, G. D. Mukherjee, M. Mezouar, and R. Boehler, J. Chem. Phys. **130**, 124509 (2009).

[10] J. W. Shaner, G. R. Gathers, and W. M. Hodgson, in *Proceedings of the Seventh Symposium on Thermophysical Properties*, edited by A. Cezairliyan, (ASME, New York, 1977), pp. 896-903.

[11] J. W. Shaner, G. R. Gathers, and C. Minichino, High Temp. High Pressures **9**, 331 (1977).

[12] A. Berthault, L. Arles, and J. Matricon, International J. Thermophysics **7**, 167 (1986).

[13] R. S. Hixson and M. A. Winkler, International J. Thermophysics **11**, 709 (1990).

[14] C. Dai, X. Jin, X. Zhou, J. Liu, and J. Hu, J. Phys. D: Appl. Phys. **34**, 3064 (2001).

[15] J. M. Brown and J. W. Shaner, in *Shock Waves in Condensed Matter – 1983*, edited by J. R. Asay, R. A. Graham, and G. K. Straub, (Elsevier, Amsterdam, 1984), pp. 91-94.

[16] C. Dai, J. Hu, and H. Tan, J. Appl. Phys. **106**, 043519 (2009).

[17] R. S. Hixson, D. A. Boness, J. W. Shaner, and J. A. Moriarty, Phys. Rev. Lett. **62**, 637 (1989).

[18] A. Strachan, T. Cagin, O. Gülseren, S. Mukherjee, R. E. Cohen, and W. A. Goddard III, Modeling Simul. Mater. Sci. Eng. **12**, S445 (2004).

[19] S. Taioli, C. Cazorla, M.J. Gillan, and D. Alfè, Phys. Rev. B **75**, 214103 (2007).

[20] Z-L. Liu, L-C. Cai, X-R. Chen, and F-Q. Jing, Phys. Rev. B **77**, 024103 (2008).

[21] J. A. Moriarty, J. N. Glosli, R. Q. Hood, J. E. Klepeis, D. A. Orlikowski, P. Söderlind, and L. H. Yang, in *TMS 2008 Annual Meeting Supplemental Proceedings Volume I: Materials Processing and Properties* (TMS, Warrendale, PA, 2008), p. 313.

[22] L. Burakovsky, S. P. Chen, D. L. Preston, A. B. Belonoshko, A. Rosengren, A. S. Mikhaylushkin, S. I. Simak, and J. A. Moriarty, Phys. Rev. Lett. **104**, 255702 (2010).

[23] C. Cazorla, M. J. Gillan, S. Taioli, and D. Alfè, J. Chem. Phys. **126**, 194502 (2007).

[24] A. B. Belonoshko, L. Burakovsky, S. P. Chen, B. Johansson, A. S. Mikhaylushkin, D. L. Preston, S. I. Simak, and D. C. Swift, Phys. Rev. Lett. **100**, 135701 (2008).

[25] J. A. Moriarty, R. Q. Hood, and L. H. Yang, Phys. Rev. Lett. **108**, 036401 (2012).

[26] W. Kohn and L. J. Sham, Phys. Rev. **140**, A1133 (1965); N. D. Mermin, Phys. Rev. **137**, A1441 (1965).

[27] C. J. Wu, P. Söderlind, J. N. Glosli, and J. E. Klepeis, Nature Mater. **8**, 223 (2009).

[28] A. Dewaele, M. Mezouar, N. Guignot, and P. Loubeyre, Phys. Rev Lett. **104**, 255701 (2010).

[29] L. L. Hsiung and D. H. Lassila, Scr. Mater. **38**, 1371 (1998); **39**, 603 (1998); Acta Mater. **48**, 4851 (2000).

[30] D. Orlikowski, P. Söderlind, and J. A. Moriarty, Phys. Rev. B **74**, 054109 (2006).

[31] P. Söderlind and J. A. Moriarty Phys. Rev. B **57**, 10340 (1998).

[32] J. A. Moriarty and J. B. Haskins (to be published).

[33] J. R. Morris, C. Z. Wang, K. M. Ho, and C. T. Chan, Phys. Rev. B **49**, 3109 (1994).

[34] A. B. Belonoshko, N. V. Skorodumova, A. Rosengren, and B. Johansson, Phys. Rev. B **73**, 012201 (2006).

[35] J. A. Moriarty Phys. Rev. B **38**, 3199 (1988).

[36] L. H. Yang, P. Söderlind, and J. A. Moriarty, Philos. Mag. A **81**, 1355 (2001).

[37] Supplemental material to Ref. [25] located online at the following internet address: http://link.aps.org/supplemental/10.1103/PhysRevLett.108.036401

[38] F. H. Streitz, J. N. Glosli, M. V. Patel, B. Chan, R. K. Yates, B. R. de Supinski, J. Sexton, and J. A. Gunnels, J. Phys.: Conf. Series **46**, 254 (2006).

[39] M. de Koning, A. Antonelli, and S. Yip, Phys. Rev. Lett. **83**, 3973 (1999).

[40] P. J. Steinhardt, D. R. Nelson, and M. Ronchetti, Phys. Rev. Lett. **47**, 1297 (1981).

[41] M. S. Daw, S. M. Foiles, and M. I. Baskes, Mater. Sci. Rep. **9**, 251 (1993).

[42] D. Alfè, C. Cazorla, and M. J. Gillan, J. Chem. Phys. **135**, 024102 (2011).

[43] A. D. B. Woods, Phys. Rev. **136**, A781 (1964).

[44] S. K. Sikka, Y. K. Vohra, and R. Chidambaram, Prog. Mater. Sci. **27**, 244 (1982).

[45] L. Burakovsky, private communication (2010).

[46] L. Burakovsky, private communication (2012).

[47] H. Park, M. R. Fellinger, T. J. Lenosky, W. W. Tipton, D. R. Trinkle, S. P. Rudin, C. Woodward, J. W. Wilkins, and R. G. Hennig, Phys. Rev. B **85**, 214121 (2012).

[48] N. C. Holmes, private communication (2012).

[49] D. H. Kalantar, J. F. Belak, G. W. Collins, J. D. Colvin, H. M. Davies, J. H. Eggert, T. C. Germann, J. Hawreliak, B. L. Holian, K. Kadau, P. S. Lomdahl, H. E. Lorenzana, M. A. Meyers, K. Rosolankova, M. S. Schneider, J. Sheppard, J. S. Stölken, and J. S. Wark, Phys. Rev. Lett. **95**, 075502 (2005).